HIGH-PERFORMANCE CHEMIRESISTOR INSTRUMENTATION CIRCUIT FOR MICRO GAS CHROMATOGRAPH

By

Xiaoyi Mu

A THESIS

Submitted to
Michigan State University
in partial fulfillment of the requirements
for the degree of

MASTER OF SCIENCE

Electrical Engineering

2011

ABSTRACT

HIGH-PERFORMANCE CHEMIRESISTOR INSTRUMENTATION CIRCUIT FOR MICRO GAS CHROMATOGRAPH

By

Xiaoyi Mu

Gas chromatography is a technology that permits detection, classification and quantification of gas and vapor mixtures, showing wide application in environmental monitoring, military surveillance, and healthcare diagnostics. Miniaturization of the gas chromatograph to a portable platform would bring significant benefits in terms of speed, sensitivity, and cost. Such a micro gas chromatograph (μGC) would open many new sensing applications that cannot be addressed by existing instruments. This thesis seeks to overcome the challenges and limitations in instrumentation circuits for a μGC detector utilizing thiolate-monolayer-protected gold nanoparticles (MPN) chemiresistor (CR) arrays. Two approaches for CR array instrumentation were explored. First, a CMOS instrumentation circuit using DC techniques was designed and tested. The 8-channel DC chip achieves a resolution better than 125ppm over a very wide baseline resistance range and 120dB dynamic range. Second, an AC instrumentation circuit was developed to overcome the noise limitations inherent to the DC circuit. In addition, a methodology for integrating CR arrays directly onto the surface of the instrumentation chip was studied and implemented to further miniaturize the μGC and maximize resolution. The results of this research lay a solid foundation for future realization of high sensitivity μGCs.

ACKNOWLEDGEMENTS

Though only my name appears on the cover of this thesis, a great many people have contributed to its production. I owe my gratitude to all those people who have made this thesis possible and because of whom my graduate experience has been one that I will cherish forever.

First of all, I would like to thank my advisor Professor Andrew Mason for his continued guidance and support through my master research. He has been a true mentor to me. I would also like to acknowledge my dissertation committee including Professor Shantanu Chakrabartty and Professor Wen Li for their valuable feedback that made this thesis possible.

I must also thank my colleagues at AMSaC lab who helped me put my ideas to practice. Special thanks to Daniel's direction, idea sharing and answering my questions. I am grateful to Xiaowen, Yue ,Garrett, Waqar, Yuning, Stefan, James, Haitao, Lin and Liya for their help. It is my pleasure to know and work with them.

I would like to thank our collaborators including Professor Zellers' group, Professor Kurdak's group and Professor Li's group. I appreciate Elizabeth, Hungwei and Forest's assistance.

Finally and most importantly, I want to thank my parents, my grandmother and my brother for believing in me and supporting me. This dissertation is dedicated to them.

Xiaoyi Mu

TABLE OF CONTENTS

LIST OF TABLES

LIST OF FIGURES

1 Introduction

1.1 Motivation

Gas chromatography is widely used in analytic chemistry for separating and analyzing mixture of compounds that can be vaporized without decomposition [1]. Nowadays, the applications of gas chromatography extend beyond the laboratory, reaching into indoor environmental monitoring, biomedical surveillance and diagnosis, and explosive detection, etc[2]. These applications require on-site rapid measurement by portable and low-cost instruments. Supported by micro-electrical-and-mechanical-system (MEMS) and CMOS fabrication processes, scaling down gas chromatographs to hand-held devices commonly referred to micro-gas-chromatograph (μGC) system is now conceivable.

The μGC consists of four main components as shown in Figure 1.1 (adapted from [3]). The micro-fabricated pre-concentrator/focuser (μPCF) collects the sample and injects into the system. Microfabricated flow columns with resistive heaters separate the samples. The sensor array detects vapors in the sample and generates electrical signals. Instrumentation electronics detect the sensor response, amplify and extract it. By fabricating the μGC components with MEMS processes and implementing the instrumentation electronics in a single-chip integrated circuit, the system can be miniaturized for on-site monitoring applications using a hand-held vapor analysis system.

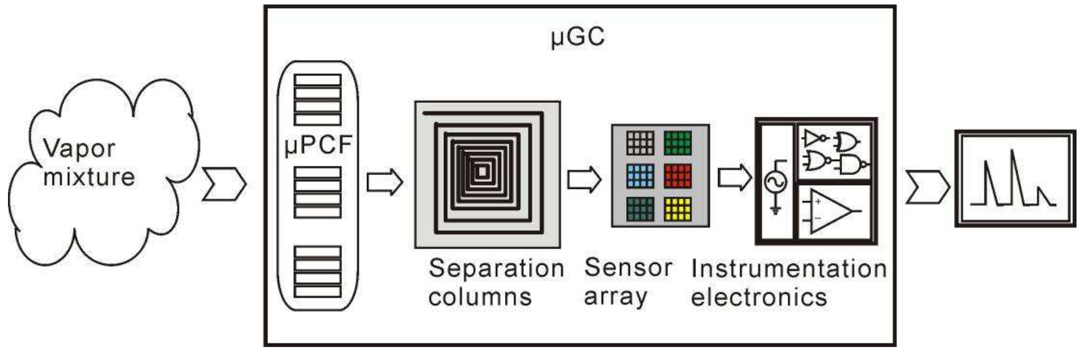

Figure 1.1. Block diagram showing the three main components in μGC. For Interpretation of the references to color in this and all other figures, the reader is referred to the electronic version of this thesis.

1.2 Challenge

The applications for μGCs often involve vapor concentration levels in the parts-per-billion (ppb) to parts-per-trillion (ppt) range, making detection of target compounds difficult. Three efforts that can help to achieve high detection limits are:

(1) Improving the concentration of analytes in μPCF by providing a focused injection pulse

(2) Adopting a high-sensitivity vapor sensor in μGC system

(3) Improving the sensitivity of the readout instrumentation circuit

Effect (1) and (2) have been achieved by our collaborator, Dr. Zellers' group in University of Michigan [3]. From the sensor point of view, chemiresistors (CR) coated with thiolate-monolayer-protected gold nanoparticles (MPN) have been demonstrated as highly sensitive vapor sensors, achieving parts-per-billion (by volume) detection limits[4]. However, to enable μGC systems to benefit from the sensitivity of MPN CR arrays, several critical limitations to CR technology need be addressed by instrumentation electronics. First, CR baseline values (the resistance before responding to a vapor) vary by up to two order of magnitude from device to device. Second, the baseline values drift over time and independently for each CR device. From a circuit point of view, all these challenges from μGC and MPN CR array can be addressed by developing a high-resolution readout circuit with large dynamic range, thus enabling μGCs to achieve the greatest possible limits of detection. Furthermore, because CRs exhibit a small capacitive response, an orthogonal measurement of vapor concentrations can potentially be incorporated into the CR array instrumentation electronics.

1.3 Goal

The goal of this project is to maximize the sensitivity and stability (accuracy over time) of sensor arrays in emerging μGC platforms by designing instrumentation circuits that fully exploit the high sensitivity of MPN-coated CR sensors while overcoming their limitations. To achieve this goal, the developed instrumentation circuitry attempts to meet the following specifications:

- Very high resolution readout of relative resistance change: target 1ppm

- Large dynamic range (support of baseline resistance values): target 100k–10MΩ

- Support multiple CR channel readout on a single chip: target 8 channels

- Low power (maximize portable μGC battery lifetime): target 100μW/channel

- Support on-chip realization of CR sensor arrays

1.4 Thesis outline

Chapter 2 describes the technology and applications of the μGC, outlines MPN CR technology, and reviews existing resistive readout methods. Chapter 3 describes the development and VLSI realization of an 8-channel DC CR instrumentation circuit for μGCs, with experimental test results and analysis in Chapter 4. Chapter 5 introduces an alternative AC CR readout design to further improve resistance resolution. In the final chapter, a summary of this thesis work and suggestions for future research are provided.

2 Background of Gas Chromatograph and Resistance Measurement

2.1 Vapor mixture analysis applications and micro gas chromatograph

Vapor mixture is a mixture of compounds that can be vaporized without decomposition. In health, environment and security regions, important information can be extracted from vapor mixture's composition and each component's concentration. By determining the ingredients and concentration, vapor mixture analysis has been adopted in health, environment and security applications including indoor monitoring, environmental tobacco smoke markers, lung cancer biomarkers, and explosive detection. The following sections will briefly introduce each application and corresponding vapor mixture analysis methodologies with their advantages and disadvantages, then introduce the μGC, a universal solution which can overcome the disadvantages.

2.1.1 Indoor vapors monitoring

Health problems associated with exposure to indoor toxic chemicals have become a growing public health concern. Many such chemicals can be classified as volatile organic compounds (VOCs), which refer to organic compounds having significant vapor pressure and affecting environment and human health. Concentrations of many VOCs are consistently higher indoors (up to ten times higher) than outdoors, which may have short-and long-term adverse health effects. Indoor VOCs mainly come from: (1) emissions from building materials [5]; (2) infiltration from outdoor air [6]; (3) human activities [7]; (4) microorganisms[8]; (5) reaction products of existing VOCs [9]. The most abundant VOCs are aliphatic and aromatic hydrocarbons, such as alkanes, benzene and toluene[10]. To further study the VOCs' health effect, it is important to determine VOCs' ingredients and concentration by vapor mixture analysis.

To date, almost all investigations of indoor VOCs mixture have adopted separate sample collections and laboratory analytical steps with the methods such as gas-chromatography/mass-spectrometry (GC-MS) [11] or gas-chromatography/ flame-ionization- detector (GC-FID) [12]. Due to the cost and delay between sampling and analysis, these conventional methods are limited in on-site monitoring, and do not allow characterization of concentration profiles with respect to spatial and temporal variations.

2.1.2 Environmental tobacco smoke markers

Exposure to environmental tobacco smoke (ETS), which is also called secondhand tobacco smoke, has been proved to cause lung cancer, heart disease and other health disorders. An estimated 3,400 lung cancer deaths and 46,000 heart disease deaths occur annually among nonsmokers in the US as a result of exposure to ETS [13]. People can be exposed to ETS in smoking-permitted environments, such as restaurants, bars and private cars. Due to the public health concerns, there is a strong need to accurately assess ETS exposure.

ETS contains a complex mixture of more than 4,000 specific components [14], among which more than 50 has been proved to individually cause cancer [13]. The complexity of ETS makes it difficult to determine ETS, prompting the use of marker compounds as surrogates for ETS detection. Vapor-phase nicotine (VPN), 3-ethenylpyridine (3-EP) and 2,5-Dimethylfuran (2,5-DMF) has been used as a biomarker of ETS [14][15]. These chemicals are often determined by GC-MS[16], GC-FID [17] and gas-chromatography with a nitrogen-phosphorus detector (GC-NPD) [18]. However, there are several disadvantages to these conventional methods: they are labor and intensive expensive, and provide less effective intervention feedback for affected individuals, which limit the potential to address the problems associated with ETS exposure.

2.1.3 Breath vapor analysis and the lung cancer biomarkers

Analysis of vapor mixture in breath can provide information about diseases and environmental exposure [19]. It is more attractive than blood analysis due to its non-invasive nature. It is the best way to directly examine respiratory function and permits real-time monitoring of volatile toxic substances in the body. The links between breath substances and diseases are currently being studied, and breath analysis may provide a useful diagnostic tool.

Lung cancer is the most common cause of cancer-related death and is responsible for 1.3 million deaths worldwide annually [13]. The overall risk of developing lung cancer during human's lifetime is 1 in 13.5. According to statistical data, survival rate for lung cancer can dramatically be increased by detection and surgical treatment at an early stage. Breath biomarker analysis is a promising lung cancer screening method [20]. VOCs such as alkanes and aromatic compounds have been found to be associated with lung cancer as breath biomarker.

To date, several methods have been utilized in breath biomarker analysis, such as GC-MS [21], GC-FID [22], and electronic nose technologies [23]. GC-MS has advantages such as high sensitivity and ability to identify compounds on the basis of their fragmentation spectra, but suffers high expense of the system and need for expertise in operation. GC-FID's use in field is prevented by its complicated system design and data analysis. Electronic nose technologies have been partially successful when applied to differentiate lung cancer patients from healthy controls, but have been judged for their inability to identify specific VOCs and low sensitivity.

2.1.4 Explosives detection

Since Sep 11 2001, explosives inspection in airports and other public areas have become more strictly enforced. Facilitating this demand requires portable, fast, high-sensitivity explosive detection instruments to replace conventional methods like trained animals. Therefore, the explosive detection techniques have been an active area of research in recent years. The United States Bureau of Alcohol, Tobacco, and Firearms [24] lists nearly 250 explosive materials, in which trinitrotoluene (TNT), hexogen (RDX) and different combinations with both of them are very powerful explosives used by terrorists. Directly detecting these ingredients is more effective and accurate than indirect way such as X-ray or metal detectors. To date, several vapor mixture analysis methods have been utilized in explosive detection, such as GC-MS [25], gas-chromatograph-ion-mobility -spectrometers (GC-IMS) [26], infrared absorption spectroscopy [27], photo-thermal deflection spectroscopy (PDS) [28], fluorescence polymer-porous silicon microcavity device [29], and thermal sensor [30]. However, due to sample's ultra low vapor pressure property and high-resolution requirement compared with general VOC detector, all of them are experimental, not yet implemented as a portable device.

2.1.5 μGC for vapor mixture analysis

The health, environment and security regions demands high-sensitivity on-site portable applications for vapor mixture analysis. However, most of the methods mentioned in previous sections hardly satisfy all the requirements. There are very few portable instruments which can analyze the components of complex vapor mixtures. These include hand-held IMS [31], hand-held mass spectrometry (MS) [32], Fourier transform infrared spectrophotometers (FTIR) [33] and μGCs. Due to the versatility associated with the ability to separate components prior to detection, compatibility with various detectors, and possibility to achieve high sensitivity, μGCs are the most promising for on-site vapor mixture monitoring and analyzing.

The μGC consists of four main components as shown in Figure 1.1. The μPCF collects the sample and injects into the system, lift the concentration in the same time. Microfabricated flow columns separate the samples with assistance of resistive heaters. The sensor array responds uniquely to different vapor composite and different concentration. Instrumentation electronics detect the sensor response, amplify and extract it. The μGC components can be fabricated with MEMS processes and the instrumentation electronics can be implemented in a single-chip integrated circuit.

The vapor mixture analysis in health, environment and security applications often involve vapor concentration levels in the parts-per-billion (ppb) to parts-per-trillion (ppt) range, making detection of target compounds difficult. Three efforts that can help to achieve high detection limits for μGC are:

(1) Improving the concentration of analytes in μPCF by providing a focused injection pulse;

(2) Adopting a high-sensitivity vapor sensor in μGC system, where chemiresistors (CR) coated with thiolate-monolayer-protected gold nanoparticles (MPN) have been

demonstrated as promising candidate;

(3) Improving the sensitivity of the readout instrumentation circuit.

2.2 CR sensor array for μGC

Various detectors have been employed in research μGC prototypes, such as micro-FID [34], PID [35], IMS [31], micro-flame photometric detector (μFPD) [36], micro-counter-flow FID [36], argon-doped helium ionization detector (HID) [37], electron capture detector (ECD) [37], micro-machined thermal conductivity detector (TCD) [38], MS [39], and chemical sensor array such as CR sensor array [40]. The complexity and high cost of these instruments limit their widespread deployment and potential in the many possible vapor mixture analysis applications.

A chemical sensor consists of a chemically selective layer which changes its physical property when interacting with incoming VOCs, and a transducer which transforms this change into electrical signal. Compared with conventional detectors used in μGC, chemical sensors have been developing rapidly and have become popular in recent years because of advantages including: low-cost of production, small size, simplicity, low power operation, and minimal maintenance [41]. Furthermore, using an array of different functional sensors, selectivity can be obtained by providing characteristic chemical ‘fingerprint’ of each analyte.

Several kinds of chemical sensors have been used as vapor detectors. These include metal-oxide semiconductor (MOX), optical, piezoelectric (e.g. SAW sensors), and chemiresistor (CR) sensors. MOX sensors are inexpensive, but suffer from performance drift and poor selectivity [42]. Optical fiber sensors, based on spectrometry measurements, offer some advantages such as electromagnetic immunity, multiplexation capability and passive operation (no bias is needed), but they are expensive [43]. Piezoelectric sensors consist of a piezoelectric substrate coating with various sensing materials; they provide good sensitivity and selectivity for chemical analytes but suffer high cost [44]. Compared with other alternatives, CR sensors are inexpensive to manufacture and have very high sensitivity that is determined by the method of chemical functionalization [45].

Carbon-doped polymers and electrically conductive polymers have been widely used as interfaces of CR sensors [46][47]. Gold-thiolate monolayer-protected nanoparticles (MPN) have arisen as promising CR interface with lower detection limits and higher sensitivity[48]. It has been reported that the MPN CR has a detection limit as good as sub-parts-per-billion (ppb) concentration of trichloroethylene in mixtures [49]. The MPNs consist of a gold core of nano-dimensions, surrounded by a monolayer of self-assembled thiolate that provide stability to the gold cores. The MPN film swells when vapor partitions diffuse into it, changing the electron tunneling barrier and thereby the film resistance. Therefore, CR response to vapors can be obtained by measuring the relative resistance change of the MPN film. A model was proposed to predict the responses of MPN-CRs based on a vapor-film partition coefficient, the analyte density and dielectric constant [50]. The model also indicates that the sensitivity of the MPN-CR depends only on vapor concentration, regardless of electrode geometry and film thickness, showing a promising possibility for miniaturization of MPN-CRs. However, MPN-CR, also introduce several challenges that must be overcome by readout circuitry:

(1) Baseline values (R_b) vary widely from device to device, typically from 100k to 10MΩ, corresponding to a dynamic baseline readout range requirement in circuit design.

(2) Baseline value drift over time independently to each device, corresponding to a drift tracking ability in circuit design.

(3) When detecting vapor such as trichloroethylene with concentration as low as sub ppb level, the sensor response ($\Delta R/R$) is quite small, as little as one part per million (ppm) [49]. To utilize the CR signal, it requires a ppm resolution readout in circuit design.

(4) CRs also exhibit a small capacitive response, potentially providing an orthogonal means of vapor measurement, corresponding to a capacitance readout requirement in circuit design.

In addition, multiple channel readout for CR array and 20Hz sampling rate are essential requirements in circuit design.

2.3 Methodologies for resistance measurement

Usually, in CR sensor measurement, current is read when a constant voltage is applied across the CR sensor film [51]. The resistance value is obtained as the voltage to current ratio. For a baseline value R_b, the CR response is defined as the normalized resistance changes ($\Delta R/ R_b$), to achieve high resolution of CR response (such as several ppm), a high-stability voltage generator and a high-resolution picoammeter are required in a laboratory environment. For example, to measure 1Ω resistance change in a 1MΩ baseline resistance, less than 1μVrms would be generated with a 1V bias applied to the CR. This would require a bias voltage stability of better than 1μVrms, which is achievable with most commercial equipment. To obtain 1μV resolution over 1V range in measurement, a picoammeter with 20-bit resolution is required, which would typically be achieved with some sort of analog-to-digital converter (ADC). Furthermore, if we consider that CR baseline values can vary from roughly 100k – 10MΩ, the required ADC resolution would be pushed up to approximately 27 bits to obtain 1ppm resolution over the whole range. Generally speaking, higher ADC resolution requires more power and chip area and significantly adds to cost. Currently, the best commercially available ADCs can only achieve 24 bits [52], so it would be impossible to achieve the required 27-bit resolution with commercial electronics.

To address this resolution challenge in CR readout, many CR interface circuits have been developed using a variety of techniques. As described below, these circuits are tailored to the performance requirements of specific CR sensor technologies that do not necessarily match the demands of MPN CR sensors.

2.3.1 Resistance-to-frequency converter

Resistance-to-frequency converter (RFC) is a method widely used by resistive gas sensors, especially for large variation of resistance [51][53-57], for example, sensors based on metal-oxide thin film have five decades in baseline value variance due to process variation [53]. RFC allows measurement of a much larger resistance range than direct linear conversion because it is not limited by voltage swing constraints in analog circuits. Figure 2.1. shows a general circuit implemented in RFC, consisting of a voltage-to-current convertor followed by an integrator, a Schmitt comparator and a digital control circuit. The current flowing in the CR alternately charges and discharges the capacitor in the integrator, the Schmitt comparator gives pulses according to integrator's output and the resulting oscillation period linearly depends on the CR value. This circuit has been reported to achieve 141dB dynamic range with a maximum accuracy of 4,000ppm over five decades [53]. However, this approach is slower than direct conversion and the accuracy is limited by parasitic capacitances to be far below MPN-CR requirements.

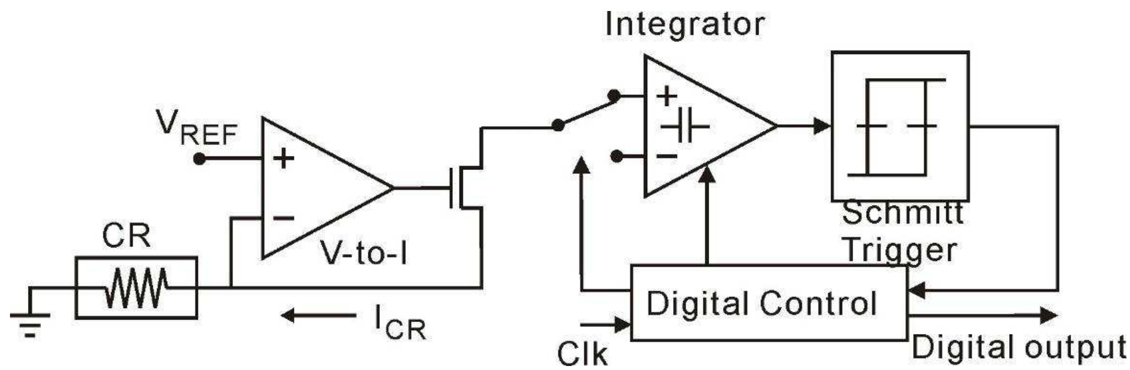

Figure 2.1. Block diagram of resistance-to-frequency conversion.

2.3.2 Logarithmic converter

The logarithmic converter is another solution to address a wide range of CR baseline values [58]. The logarithmic converter is typically implemented with a voltage-to-current converter and a pair of diode-connected vertical PNP transistors as shown in Figure 2.2. The difference of the two bipolars' emitter-base voltage V_{EB1} & V_{EB2} can be expressed as:

$$\begin{aligned}\Delta V_{EB} &= V_{EB1} - V_{EB2} = \frac{kT}{q}\ln\left(\frac{I_R}{I_{REF}}\right) \\ &= -\frac{kT}{q}\ln\left(R_{CR}\frac{I_{REF}}{V_{CM}}\right)\end{aligned} \tag{2.1}$$

where k is he Boltzmann constant, q is the electron charge, T is the absolute temperature on the chip, I_{REF} is a reference current, I_R is the output current of the voltage-to-current converter, and the V_{CM} is the common-mode voltage of the logarithmic converter. Therefore, the differential output ΔV_{EB} is logarithmic related with CR resistance value (R_{CR}). This method can provide five decades of dynamic range (1kΩ – 10MΩ). However, because of the nonidealities in CMOS parasitic vertical bipolar devices, only 10,000ppm resolution ($\Delta R/R_b$) is achieved. This resolution does not satisfy MPN-CR's requirements (~1ppm).

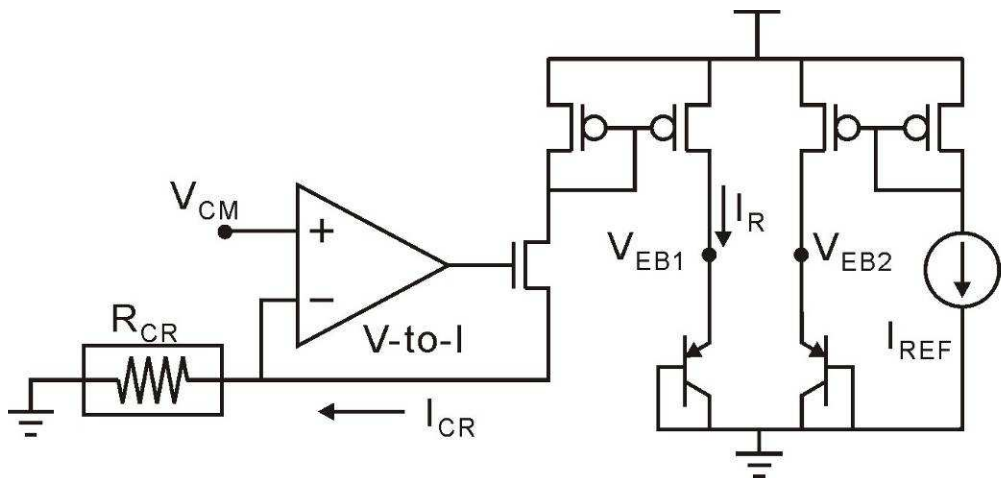

Figure 2.2. Logarithmic converter for readout a CR with a wide resistance change.

2.3.3 Multi-scale current-to-voltage converter

Another method to address the wide CR resistance range involving a multi-scale current-to-voltage converter was proposed [59]. This readout circuit is composed of a single-ended continuous-time programmable transresistance amplifier (PTA) and a 13-bit ADC as shown in Figure 2.3. The PTA converts the current flowing through the sensor into a voltage and the 13-bit ADC digitizes the output of the PTA. To accommodate a five-decade range of baseline values, this system also requires two 8-bit digital-to-analog convertors (DAC) and a digital signal processor (DSP) for control and calibration. This readout circuit can measure a sensor resistance range of more than five decades (100Ω-20MΩ) and achieve a resolution of better than 1000ppm which does not satisfy MPN-CR's resolution requirement.

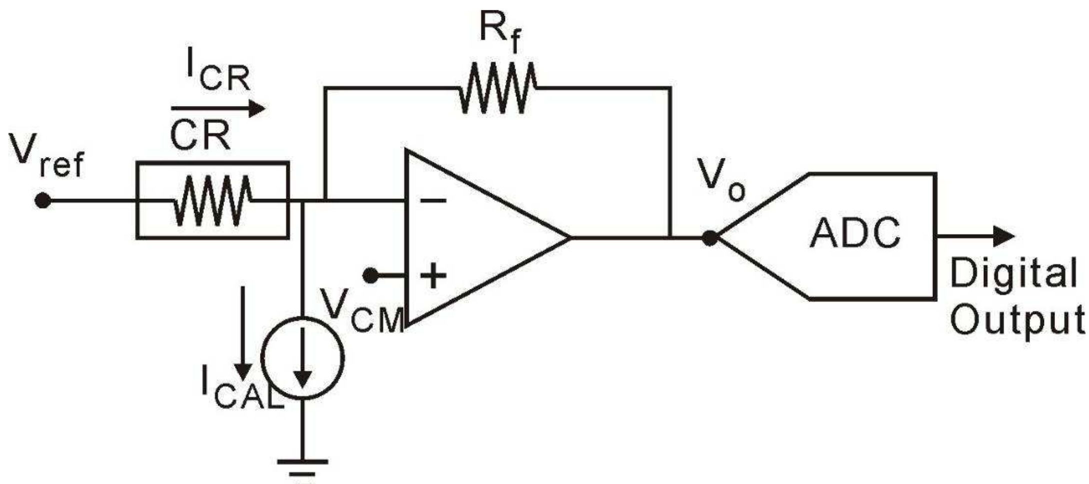

Figure 2.3. Block diagram of multi-scale current-to-voltage converter.

2.3.4 Baseline cancellation methodology

To achieve high resolution of CR response, baseline cancellation method was proposed recently[60]. The working principle and benefit are described below.

As mentioned in the first paragraph of section 2.3, small CR response requires high ADC resolution in direct linear conversion. The reason is that when the entire sensor value (baseline plus response) is digitized, ΔR receives only a small portion of the ADC's resolution. In other words, the resolution available to digitize ΔR is very small. If, however, R_b is first canceled and ΔR is amplified before digitizing, the full resolution of the ADC may be used. Figure 2.4 shows an illustration of this baseline cancellation principle. Given a gain of A, extra $\log_2(A)$ bits of resolution is provide compared to the direct linear conversion. In this way, the requirement for ADC's resolution is loosed and the complexity of ADC is dramatically decreased. For example, to measure 1Ω resistance change in a 1MΩ baseline resistance, direct linear conversion need 20-bit ADC; in contrast, by baseline cancellation and amplifying ΔR 64 times, only 14-bit ADC is required.

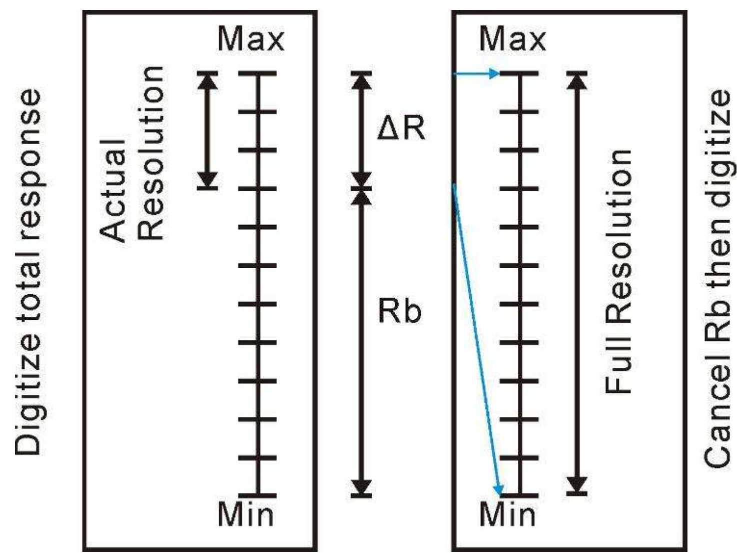

Figure 2.4. Illustration of baseline cancellation principle.

Several interface circuits have been developed in baseline cancellation method. Amplifying differential signal between an active CR and a passivated (non-sensing) element can achieve a resolution better than the noise floor of CR itself [61]. However, this approach has limited utility because fabricating two sensors with identical initial baseline and drift characteristics is nearly impossible with most sensor technologies. Alternatively, baseline cancellation using an op-amp with resistive feedback and a power gain stage has been reported to provide a resolution ($\Delta R / R_b$) of about 200ppm [60]. However, it does not provide drift tracking.

2.3.5 Methodologies summary

In section 2.3, the methodologies for CR readout were reviewed. Although resistance-to-frequency converter and logarithmic converters can provide large dynamic range, they only achieve limited resolution ~ 10,000ppm. In comparison multi-scale current-to-voltage converter is better in dynamic range and resolution, but still does not satisfy the MPN-CR resolution specification. Baseline cancellation methodology provides a promising way to push down the resolution. Our prior work shows a baseline cancellation and tracking approach for MPN-CR readout [62], in which a cancellation and amplification circuit was implemented in IC. In the next chapter, a fully integrated baseline cancellation system based on [62] will be presented, targeting the goals listed in Chapter 1.

3 DC Chemiresistor Instrumentation Circuit Design

3.1 Requirement and approach for high sensitivity

The normalized resistance change ($\Delta R/R_b$) of a CR sensor is directly related to the concentration of target vapors. However, the desired response portion of the sensor ΔR is small and buried within the large total value $\Delta R + R_b$. Furthermore, R_b varies widely from sensor to sensor in two orders of magnitude. To acquire $\Delta R/ R_b$ with high resolution, the readout circuit must both overcome the large variation of R_b and precisely measure small ΔR values. In our lab's prior work [62] we introduced a baseline resistance cancelation approach that subtracts R_b from the total CR resistance, amplifies and digitizes the ΔR portion. The readout range and resolution of ΔR are limited by how accurately R_b is measured and subtracted and how large the ΔR is amplified. Thus, tracking R_b values closely is important over the wide dynamic range typical CR sensors present. Canceling R_b in the analog domain and amplifying only ΔR significantly improves the overall signal to noise ratio (SNR).

To meet these requirements, the architecture for the CR instrumentation circuit (one channel) is shown in Figure 3.1. The CR sensor is stimulated by a constant bias current I_R, and the sensor voltage response is

$$V_{sens} = I_R R_{sens}. \qquad (3.1)$$

where $R_{sens} = \Delta R + R_b$. The circuit works in two phases. In the idle phase (ΔR=0), a calibration is performed to determine the bias current such that the voltage drop on CR sensor $V_{sens1} = I_R \cdot R_b$ is between V_{min} and V_{max}. Because R_b can vary by more than two orders of magnitude, this large resistance range needs to be mapped into a small voltage range by adjusting the programmable current bias. The determined value of V_{sens1} is then stored on the analog memory (AM) to end the idle (calibration) phase.

During the response phase when CR is exposed to the target vapor, the voltage drop on CR sensor changes to $V_{sen2} = I_R \cdot (R_b + \Delta R)$ and is input to the subtraction and gain block. This block removes the baseline value V_{sens1} (previously stored on the AM) from V_{sens2}, amplifies the difference, and outputs only the sensor response with a gain of A. After these two phases, V_{sens1} and $A(V_{sens2} - V_{sens1})$ are obtained, corresponding to R_b and $A\Delta R$. With subsequent A/D conversion and offline calculations, $\Delta R/ R_b$ can readily be obtained from $V_{sens1}/A(V_{sens2}- V_{sens1})$. The scale A provides extra $\log_2(A)$ bits of resolution compared to the direct linear conversion. Because the ΔR signal is very small and susceptible to noise, the subtraction and gain block is fully differential to minimize common mode noise. Input offsets of the subtraction and gain block are eliminated by this sample and subtract process.

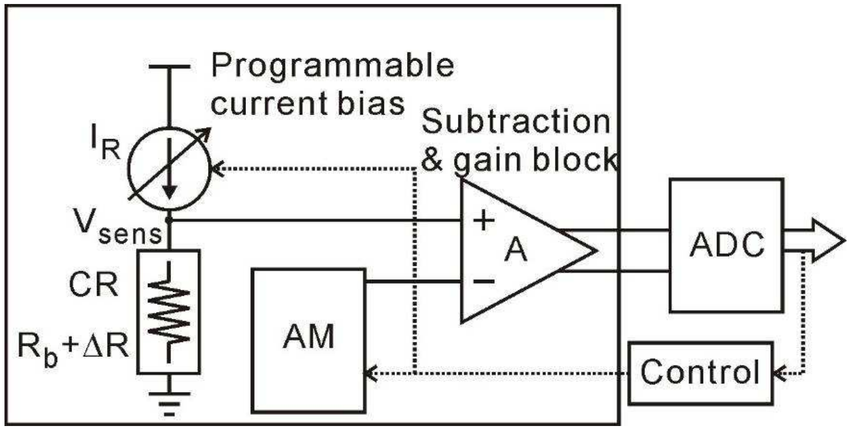

Figure 3.1. Single channel architecture for CR baseline tracking and cancellation.

3.2 Circuit implementation

The CR baseline tracking and cancellation approach first described in [62] has been significantly expanded and improved in the 8-channel circuit. This fully integrated CR instrumentation system contains a wide-range programmable exponential current bias, an 8-bit DAC for the AM, a subtraction and gain block, a digital communication and control circuit, and surface contacts to support an on-chip MPN CR sensor array.

3.2.1 Programmable exponential current bias

The normalized resistance change ($\Delta R/ R_b$) of the MPN-coated CR sensor is proportional to the concentration of target vapors. And, the ratio of $\Delta R/ R_b$ to vapor concentration is independent of the baseline R_b. Because R_b varies from 100kΩ to 10MΩ from sensor to senor, 2 order of magnitude variation of ΔR will be observed when sensing the same analyte. With a fixed current bias, (V_{sens2} - V_{sens1}) could vary in the same magnitude of ΔR, giving a tremendously variable resolution of $\Delta R/R_b$. To extract the same level of $\Delta R/R_b$ resolution for all values of R_b, a programmable current bias is essential for mapping baseline resistance into a narrow output voltage range, V_b.

Assuming that the range of voltage V_b is held within V_{min} to V_{max} by the current bias and that the discrete programmable current is I[n], where n is number of current values available, the current values I[n] provided by the system must be set such that

$$V_{\min} \le I[n]R_b \le V_{\max} \tag{3.2}$$

In other words, for all values of R_b, a current I[n] should be available such that the conditions in (3.2) are met. To ensure all possible R_b values generate a voltage between V_{min} and V_{max}, the V_b steps for each I[n] must overlap. This can be expressed mathematically as

$$\frac{V_{\min}}{I[n]} \le \frac{V_{\max}}{I[n-1]} \quad , \quad \frac{V_{\max}}{I[n+1]} \le \frac{V_{\min}}{I[n]} \tag{3.3}$$

When the boundary values of adjacent steps are set equal to each other, (3.3) becomes

$$\frac{I[n]}{I[n-1]} = \frac{I[n+1]}{I[n]} = \alpha \tag{3.4}$$

So I[n] can be derived as

$$I[n] = I[1]^{\alpha \cdot n} \tag{3.5}$$

This indicates that an exponential current bias would best span the required range with the fewest steps.

The current bias circuit shown in Figure 3.2 was designed to achieve this goal. The lower five control bits tune the current scaling in 22 exponential steps, from 1 to 1.1^{21} (=7.4). The higher two control bits provide coarse steps via programmable current gain with values of 1, 5 and 25. The exponential ratio is chosen as 1.1 to keep V_b range in [0.62V, 0.72V] with overlap between adjacent steps, contributing AM DAC extra 2 bits resolution. The coarse step extends the exponential current range to 2 orders, in the meantime guarantees overlap between adjacent steps. The monotonicity in range selection is not critical because the current only changes during calibration and for each set of ΔR and R_b measurements, the current is fixed.

Noise and mismatch need to be taken into consideration in the design point of view. First, the noise comes primarily from current source and the CR. The thermal noise of a normal resistor R can be shown as

$$\overline{v^2{}_R} = 4kTR\Delta f \tag{3.6}$$

where k is Boltzmann's constant, equals to $1.38\text{x}10^{-23}$ J/K; T is the temperature, Δf is the bandwidth. For a single transistor current source, the noise is composed of thermal noise and flicker noise, shown as

$$\overline{v^2}_M = 4kT(\frac{2}{3}g_m)R^2\Delta f + \frac{K}{C_{OX}WL}\ln\frac{f_h}{f_l} \tag{3.7}$$

where g_m is the transistor's transconductance, C_{OX} is unit capacitance of the transistor's thin oxide, W is the width of transistor gate, L is the length of the transistor gate, K is flicker noise constant(related with the process), f_h is the up boundary of frequency bandwidth and f_l is the lower boundary. (3.6) and (3.7) indicate that to reach low noise level, small R, small g_m and large W and L are preferred. Because the bias current is constant, the flicker noise dominates the noise sources. Thus the main effect to eliminate the noise is to enlarge W and L. In the meantime, low mismatch also benefits from the large transistor design.

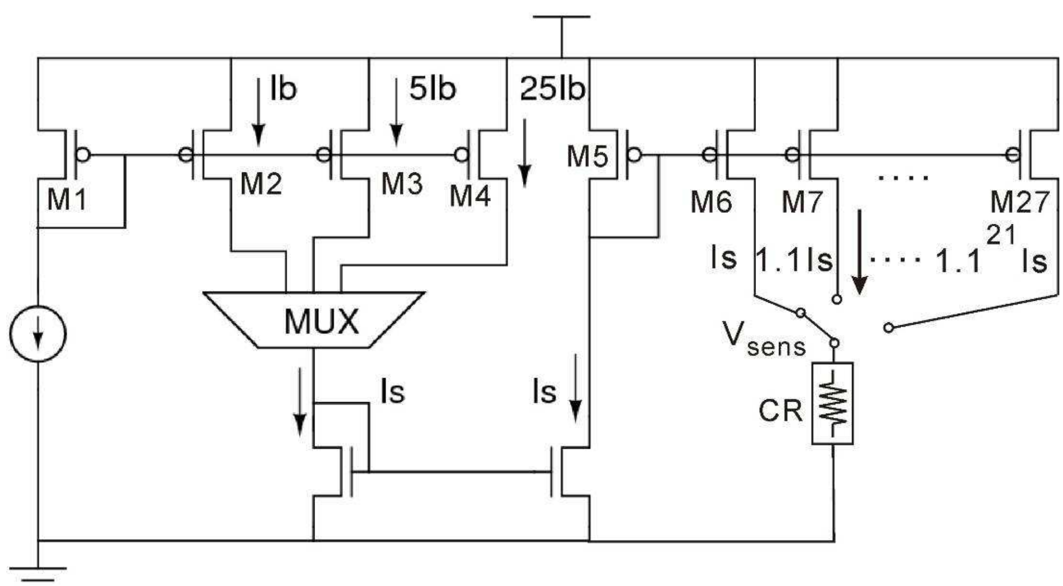

Figure 3.2. Schematic of wide-range programmable exponential current bias.

In the current bias circuit design, transistors M6 to M27 have a large width and length to minimize flicker noise, reduce errors due to process mismatch, and bolster output resistance. The current variations caused by variable V_{sens} are negligible (only 0.1% in simulation) because M6 to M27 have a large gate length and their drain voltages are narrowly held between V_{max} and V_{min}.

As shown in Figure 3.3, the total tunable range of current is from 60nA to 12.7μA, which keeps V_b between 0.62V (V_{min}) and 0.72V (V_{max}) for all values of R_b between 48.6kΩ to 12MΩ. The three coarse steps of current have overlap, guarantees continuous coverage when tuning higher two bits. Figure 3.4 shows that adjacent steps of current have overlap in resistance range, which guarantees continuous coverage over the whole range.

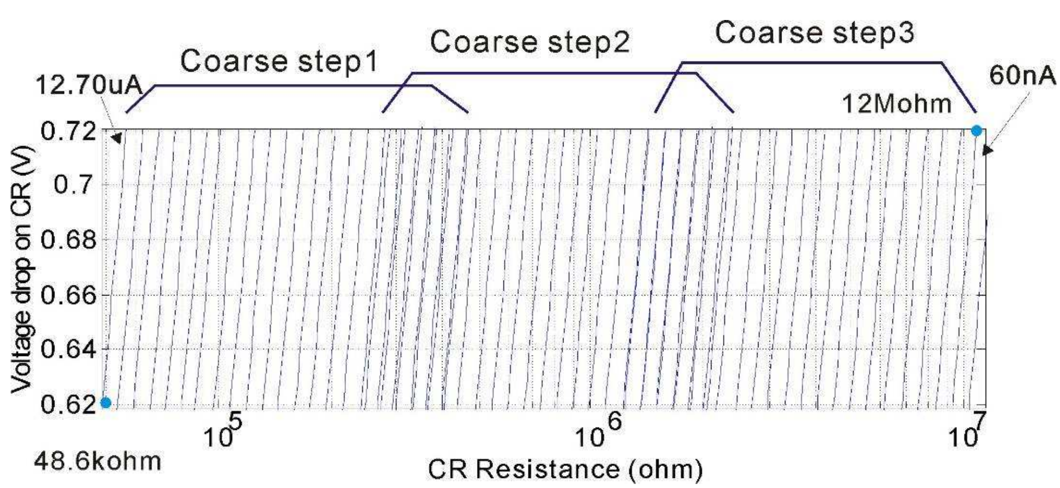

Figure 3.3. Post-layout simulation results show CR resistance is mapped to V_b by multi-scale currents. By choosing a proper current value, any CR resistance value between 48.6kΩ to 12MΩ can generate a voltage drop between 0.62V to 0.72V. The three coarse steps of current set show overlap in the figure.

3.2.2 Analog memory

To achieve high resolution measurement of the sensor's response, an analog memory (AM) is utilized to store the baseline output value (V_b) and subsequently subtract this offset value during sensor readout. A simple calibration routine is used to set the value in the AM. When the sensor is idle ($\Delta R=0$), the readout circuit output should ideally be 0V. During calibration, a feedback loop from the amplifier output to the AM is used to drive the output to 0V. Calibration is complete once this state is achieved, and thus the AM will hold the proper baseline value. This approach also has the advantage of compensating for all non-ideal offsets in the base cancellation and gain blocks shown in Figure 3.1.

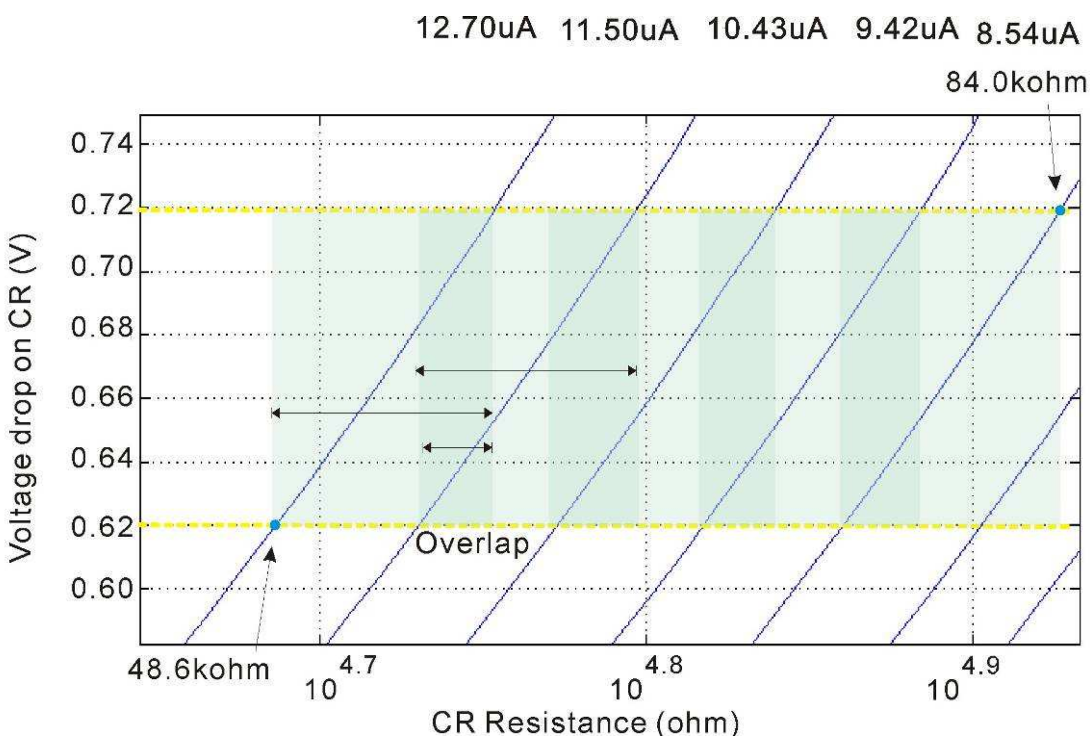

Figure 3.4. Partial plots of Figure 3.4. Each scale of current has overlap in resistance coverage, which guarantees continuous coverage over the whole range in regardless of layout mismatch or channel length modulation.

The baseline resistances of MPN CRs are known to drift significantly within a matter of minutes. Ideally the readout system should support a drift tracking re-calibration scheme. Our targeted MPN CRs are typically implemented within a μGC system [40] that periodically analyzes pre-concentrated vapor samples and permits regular recalibration in a clear environment. Because the time between recalibration periods is on the order of minutes, charge leakage excludes the use of a capacitor-based AM. Therefore, the AM was implemented as a digital to analog converter (DAC) that can hold the AM value indefinitely. Note that after calibration, the AM-DAC holds the digital value of R_b so it is readily available to determine $\Delta R/R_b$.

The disadvantage of a DAC-based AM is that it stores a discrete estimate of the baseline resistance. The AM output voltage can be expressed as

$$V_{AM} = I_R R_b' \tag{3.8}$$

where R_b' is the DAC estimate of R_b, $I_R R_b'$ is within one LSB of the actual $I_R R_b$ To determine the necessary resolution of the DAC, consider that the baseline cancellation error, ε, can be expressed by

$$\varepsilon = I_R\left(R_b - R_b'\right) \leq \frac{V_h - V_l}{2^N} \tag{3.9}$$

where V_h to V_l is the output range of the DAC and N is the DAC bit resolution. During calibration, the output never reaches exactly 0V due to ε. Thus, if higher precision is required, ε can be recorded during calibration and used in post processing the data. The primary restriction on ε is that it should not exceed the input range of the amplifier. Because the programmable current bias already limits Vb to 0.62 - 0.72V, the DAC is just need to span this range for AM control. It was determined that an 8-bit R-2R ladder current-mode DAC limits the output error to less than 1mV and satisfies the requirement set by (3.9). The resistor-based DAC shown in Figure 3.5 was implemented and holds the output indefinitely without ripple.

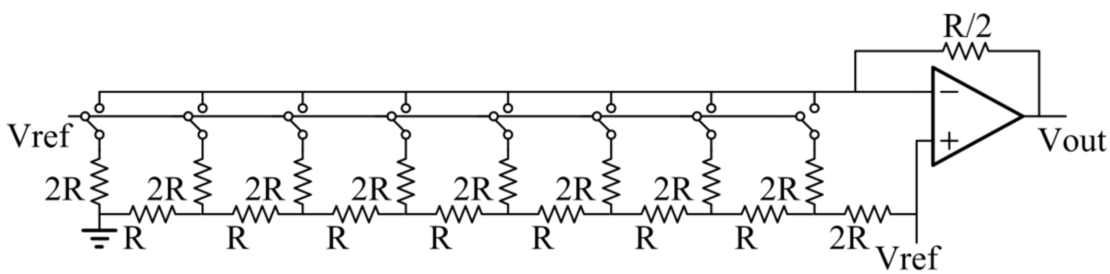

Figure 3.5. R-2R ladder current-mode 8-bit DAC schematic. Setting Vref to 0.6V sets Vout to match V_b.

3.2.3 Subtraction and gain block

To achieve high resolution measurement of the sensor's response, R_b is cancelled and only ΔR is amplified by the subtraction and gain block. The subtraction and gain block needs good linearity over the readout range and programmable gain set to match the dynamic range of the sensor during operation. It was implemented using the fully differential amplifier shown in Figure 3.6. The first stage is an operational transconductance amplifier (OTA), with g_m=1/R_s. High input impedance and fully differential structure minimize the noise and area compared to the conventional closed-loop operational amplifier with buffer design. The second stage is a closed loop amplifier. The total gain is $A = g_m \cdot R_d = R_d / R_s$. Gain accuracy is ensured by careful resistance matching in the layout and the gain linearity is ensured by fixing common-mode voltage at the input of the second stage. Three different values of R_s are designed to select, in able to provide programmable gain from 20 to 320. With external 16bit A/D conversion, at least 20bit resolution of $\Delta R/ R_b$ could be achieved based on baseline cancellation principle, satisfies the design goal (1ppm) mentioned in Chapter 2.

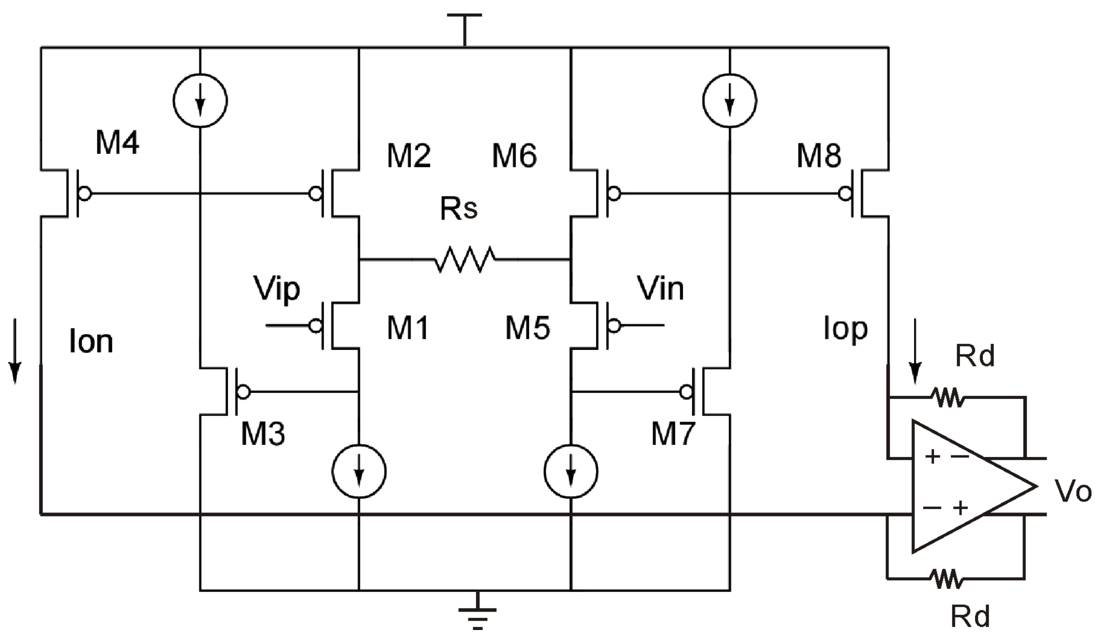

Figure 3.6. Subtraction and gain block with a total gain of R_d/R_s.

3.2.4 Digital control and communication block

To provide programmable configurations and communication with the computer, digital control and communication block is utilized in the circuit. The schematic of the 8-channel CR instrumentation circuit is shown in Figure 3.7 with digitally controlled AM DAC, programmable current bias, amplifier gain, and channel selection. The channel multiplexer was inserted between OTA and the second stage of subtraction and gain block. By placing the second stage after channel multiplexer, only one amplifier is needed, saving power and area. A 6-byte memory was implemented along with a serial peripheral interface (SPI) communication block to minimize the number of I/O pins required. Serial data are fed into the SPI and stored into memory registers to configure the settings for all analog circuits.

3.2.5 Compatibility with on-chip CR array

There are significant advantages to integrating CR array directly on the surface of the instrumentation chip, including elimination of most sources of environmental noise and miniaturization of the detector sub-system of the μGC platform. However, two important challenges need to be addressed in order to achieve this goal.

First, experimental efforts to form interdigitated electrodes for MPN sensors on the surface of CMOS chips demonstrated a problem related to the flatness of the chip's surface. Because the MPN-CR sensor electrodes are formed using very thin metal layers, they require an extremely flat surface to avoid trace discontinuities in the electrodes and their connections to on-chip contact openings. However, most CMOS processes, including AMI 0.5μm process used in this research, do not planarize the surface after the top-most metallization, and any top metal routing would create sharp surface topography.

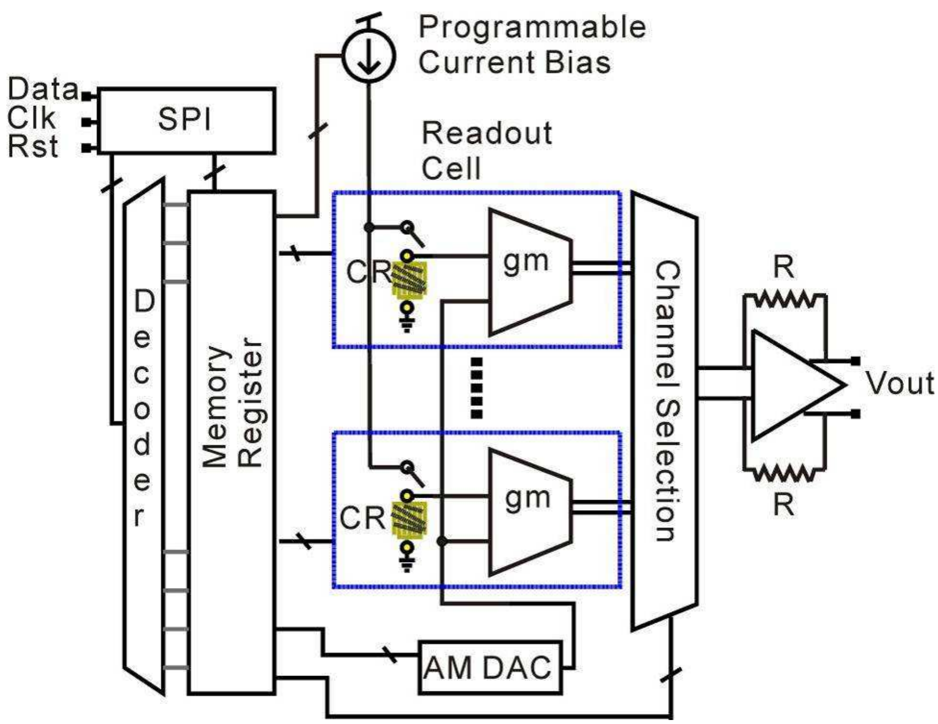

Figure 3.7. Schematic of the 8-channel CR instrumentation circuit that integrates subtraction and gain cells, an analog memory DAC, a programmable current bias and a digital control and communication block.

To solve this issue, there are two primary options that avoid additional process steps to planarize the chip's surface. One is to eliminate any top metal routing within the sensor area, and the other is to cover the entire sensor area with the top metal layer. In order to address the issue below, the second option was chosen and a metal3 plateau was formed beneath the sensor electrode area.

Second, the electron beam lithography (EBL) that was used in CR fabrication was observed to cause defects the circuit beneath the sensor area exposure to EBL. The defect principle can be explained as following: (1) High-energy electron beam can stimulate the electron-hole pairs in thin gate oxide. Compared to the higher mobility of electrons, holes have relatively higher probability to be trapped in the oxide defects and to form positive charge in the gate [63]. (2) Electron beam accumulates at the gate to induce negative voltage. Under the high electric field, great deal of majority carrier holes are accumulated at the Si/SiO_2 interface and a very small proportion of these holes have enough of the energy to enter into the gate oxide and been trapped there [64]. The trapped charge Q_{ss} affects transistor's threshold voltage shift ΔV_{th}, which is shown

$$\Delta V_{th} = -\frac{Q_{ss}}{C_{OX}} \tag{3.10}$$

The extra charge trapped in the gate oxide shifts the transistor's threshold, causing the whole analog block's failure.

To solve this problem, several options were identified. Annealing has been shown to be a promising solution to remove the trapped charge [63]. Alternatively, grounded metal layer shows a possible solution to isolate the substrate from EBL effect. Finally, because high-energy electrons travel only a very limited distance (~10μm) from their point of impact, the EBL exposure region can be physically separated from the circuit region without losing significant silicon area.

To evaluate the effect of the EBL on circuit and verify the potential solutions mentioned above, a test chip with transistor array was designed and exposed under 30keV electron beam with dose of 150μC/cm^2. Figure 3.8. (a) shows three transistors' threshold voltage shift after EBL. The first transistor does not have metal covered while the left two have either one layer or two layers of metal covered and grounded in EBL process. All of them have significant threshold shift, indicating the grounded metal cannot isolate the high-energy electrons. Figure 3.8.(b) shows the threshold voltage shift of a transistor after EBL exposure and then annealing for 8 hour at 200C temperature. The annealing can attenuate but cannot eliminate the EBL effect. Figure 3.8.(c) shows the threshold voltage shift of three transistors with different locations from the exposure spot. The results point out that the farther the circuit area is from the sensor area, the less effect on transistor's threshold shift. Placing transistors 120μm away from exposure spot would be safe. In conclusion, the best solution is to separate the circuit region from CR array region and 120μm is a conservative value.

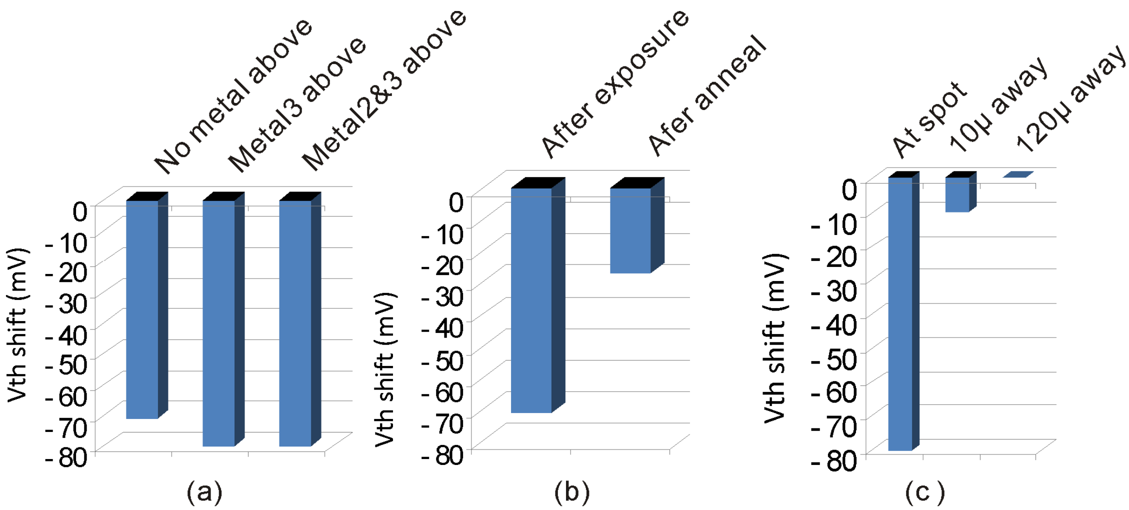

Figure 3.8. (a) Threshold voltage shift of three transistors after EBL exposure. The first transistor does not have metal covered while the left two have either one layer or two layers of metal covered and grounded in EBL process. (b) Threshold voltage shift of a transistor after EBL exposure and then annealing for 8 hour at 200C temperature. (c) The threshold voltage shift of three transistors with different locations from the exposure spot.

4 DC Instrumentation Results and Analysis

4.1 CMOS implementation

The 8-channel DC CR-array instrumentation circuit was fabricated in AMI 0.5μm CMOS process. It uses a 3.3V power supply and consumes 66μW per channel. The die photo of the 2.2×2.2mm chip is shown in Figure 4.1 with the main functional blocks labeled. The electrode area with metal3 layer underneath permits direct connection between on-chip circuitry and interdigitated electrodes patterned on the chip's surface using electron-beam lithography. To avoid damage to circuitry from post-CMOS electron-beam lithography, the sensor array (electrode contact) area contains no circuitry. All the functional circuits are placed far from the electrode area. The sensor area is placed in the middle of the chip to facilitate post-wire-bonding application of a PDMS "cap" that creates a microfluidic cell on the surface of the chip.

4.2 CR instrumentation circuit performance characterization

4.2.1 Experiment setup

A data acquisition card (DAQ PCI-6259) from Agilent Technologies was used to interface the CR-array readout chip with a PC running LabVIEW to configure and control the chip. The setup is shown in Figure 4.2. The DAQ PCI-6259 can generate digital control signals for the chip, acquire the analog signals from the chip, digitize, display and store data in the PC. The chip, the DAQ connector block and the battery are placed in a metal shielding box to isolate environment noise. A standard carbon film resistor as simulated CR is used to characterize the chip's performance.

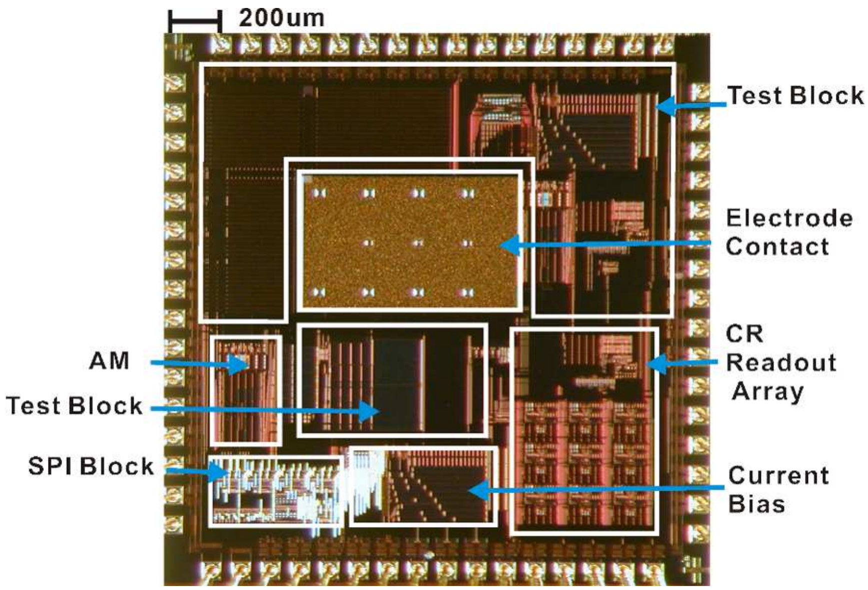

Figure 4.1. Die photo of 2.2×2.2mm CR-array readout chip.

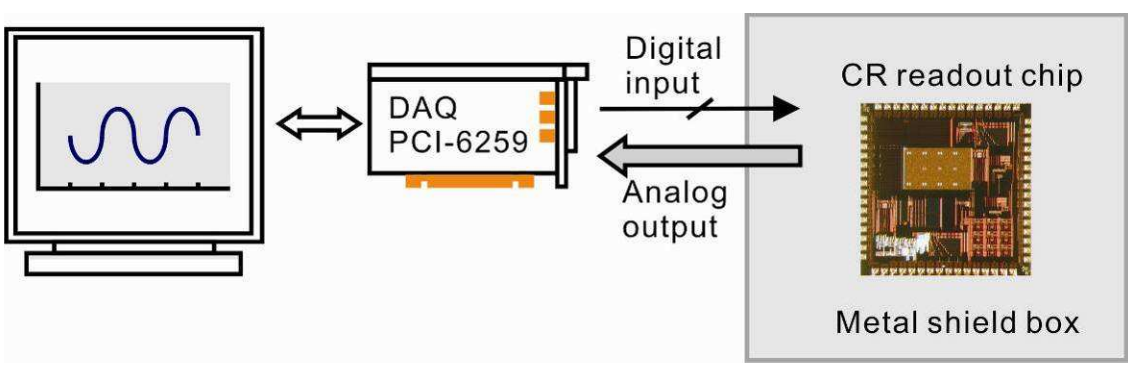

Figure 4.2. Experiment setup diagram for CR instrumentation circuit performance characterization.

4.2.2 Characteristics of programmable exponential current bias

To characterize the performance of the programmable exponential current bias, the baseline resistance was swept over a large range and the current bias was periodically re-programmed to minimize the V_b range. V_b was recorded in terms of CR resistance change and is shown in Figure 4.3, The result indicates that V_b can be held within the tight range of 0.61 - 0.72V for all values of R_b from 52kΩ to 13.28MΩ. Compared to the design specification setting in 3.2.1, which is to keep V_b between 0.62V and 0.72V for R_b between 48.6kΩ to 12MΩ, the result approximately meets the requirement.

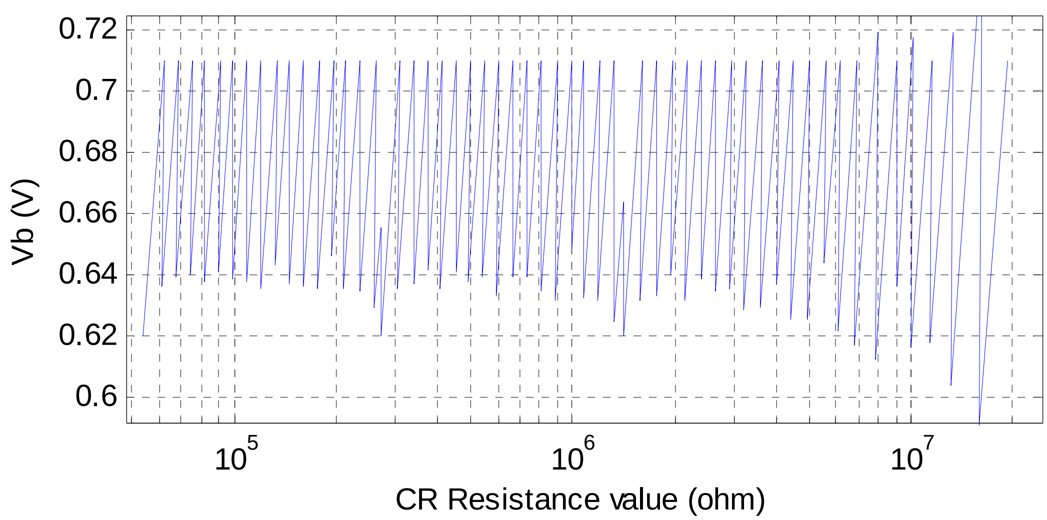

Figure 4.3. V_b vs. CR value by tuning the programmable current bias.

4.2.3 Characteristics of AM DAC

To characterize the performance of the AM DAC, 8-bit control input was swept from 1 to 255. Recall that the current bias was designed to maintain V_b between 0.61 – 0.72V; the job of the DAC is to span this range for AM control. Figure 4.4 (a) shows that the output range of DAC is 0.6 – 0.75V, meeting the design requirement.

The DAC was designed to achieve an accuracy of 8 bit. The integral nonlinearity (INL) and differential nonlinearity (DNL) of the DAC were calculated from the measured step error in the Figure 4.4. (a) data. Figure 4.4. (b) shows that the INL and DNL are lower than -50dB for all DAC input codes. Since -48dB is equal to 8-bit resolution, the DAC achieves the designed resolution.

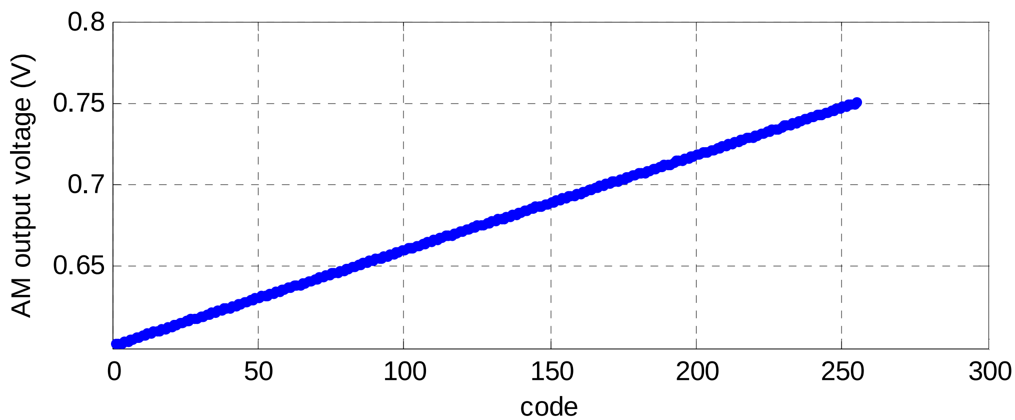

(a)

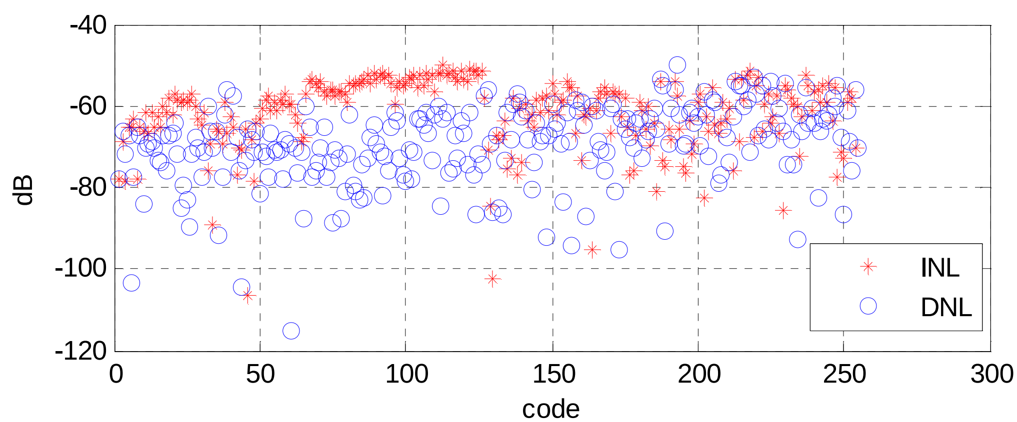

(b)

Figure 4.4. (a) The output range of DAC. (b) The INL and DNL of DAC.

4.2.4 Characteristics of subtraction and gain block

To characterize the performance of the subtraction and gain block, the input voltage of this block was swept near the operational point of the OTA and the voltage transfer function of this block was acquired. The gain, the differential input range and the linearity were calculated from the data at three gain settings; subsequently, the extra resolution bits contribution and the readout range in terms of ΔR/R were derived. Table 4.1. lists the performance of the subtraction and grain block. The result shows that the linearity is good over the programmable gain range. Recall that the gain is optional to accommodate the dynamic range of the sensor during the CR array test. By choosing low gain, the CR instrumentation chip can readout ΔR as large as +/- 12.6% of R_b with extra 4 bits resolution; by choosing high gain, the CR instrumentation chip can provide as high as 8.3 extra bits resolution with +/- 0.7% ΔR/ R_b.

Gain	17.7	85	325
Extra resolution bits ($\log_2$(gain))	4.1	6.4	8.3
Input range(+/-) (mV)	85	16.4	4.9
Readout range of ΔR/R (+/-)	12.6%	2.4%	0.7%
Linearity (R-square)	0.9999997	0.9999996	0.9999960

Table 4.1. Subtraction and gain block performance summary.

4.2.5 Characteristics of the CR-array instrumentation chip

The resolution of a signal is commonly defined as 6 times the standard deviation (σ) of the signal noise level. This definition has been adopted to establish the ΔR/R resolution.

Chip readout output was measured 1000 times for a fixed sensor resistance (input) and the standard deviation of the collected output values was calculated. In this manner, by sweeping resistance from 60kΩ to 10MΩ, the chip resolution vs. CR resistance was obtained as plotted in Figure 4.5. The resolution was found to be better than 125ppm over the resistance range. Notice that the resolution (in ppm) is lowest (best) for low values of resistance and increases (gets worse) as resistance increases. This agrees with analysis in Chapter 3, Equation 3.6 and 3.7, showing that the first two noise terms are related with resistance value.

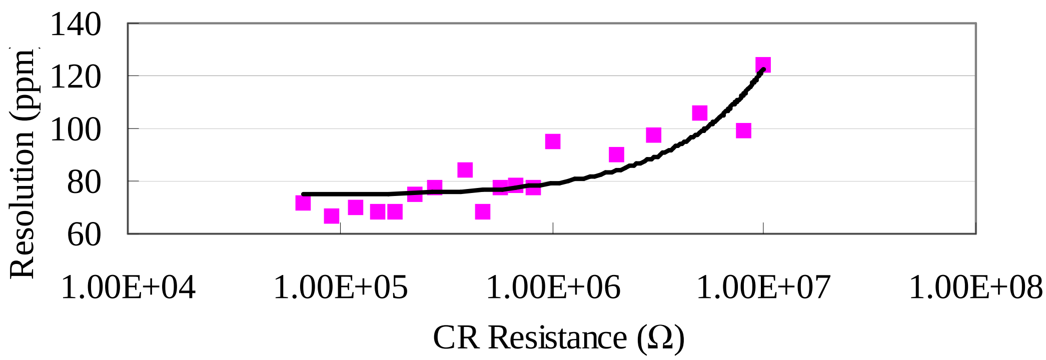

Figure 4.5. CR instrumentation circuit readout resolution vs. CR resistance value.

4.2.6 Discussion

The above experiment shows that the CR instrumentation circuit is able to cancel the baseline from 60k to 10M and provide $\Delta R/ R_b$ resolution better than 125ppm over the whole baseline range. In terms of the baseline coverage range and resolution over the whole baseline range, the circuit achieves equivalent 120dB dynamic range. Table 4.2.

shows a comparison of resistive readout methodologies. It should be noticed that our previous approach [64] can achieve the resolution 57ppm only after 5Hz low pass filter, however, is not fitting the speed requirement of μGC (20Hz). Although the test result hasn't meet the 1ppm goal listed in Chapter1, this instrumentation circuit's resolution is better than other approaches and provides large dynamic range as well.

Methodology	Resolution (ΔR/R)	Baseline range	Dynamic range
Resistance-to-frequency converter [55]	4000ppm	five decades	141dB
Logarithmic converter [60]	10,000ppm	1kΩ – 10MΩ	x
Multi-scale I-to-V converter [61]	1000ppm	100Ω-20MΩ	160dB
Baseline cancellation methodology [63]	200ppm	x	x
Baseline cancellation methodology [64]	57ppm	x	x
Our approach	60ppm-125ppm	60kΩ-10MΩ	120dB

Table 4.2. Comparison of CR instrumentation circuit's performance with other approaches.

4.3 CR sensor array measurement

4.3.1 Experiment setup

Having verified and characterized the performance of the DC CR instrumentation circuit with fix resistance values, the next step is to perform vapor chamber tests with an MPN-CR array to demonstrate the chip's capabilities for baseline cancellation, drift tracking and multi-channel supporting and characterize the linearity. To test the CR array chip under real conditions, a prototype CR readout system was developed. The electrical part was adapted from the chip characterization test platform. The CR instrumentation chip is connected to an MPN-CR sensor array, as shown in Figure 4.6. A customized small PCB （3.6inch x 2.7inch） shown in Figure 4.7 was designed to be able to hold both the chip and the CR array, and to fit in the test chamber as well. A user interface was implemented using LabVIEW, providing a customized setup and a virtual oscilloscope, as shown in Figure 4.8.

Through this chamber, the target vapor was alternately dosed in a controlled concentration with a dosing phase of 5 minutes and a passive vapor during recovering phase for 5 minutes. A 1-mercapto-6-phenoxyhexane (OPH)-thiolated MPN-coated CR array was tested in two common breath VOCs as lung cancer biomark, toluene and 2-butanone.

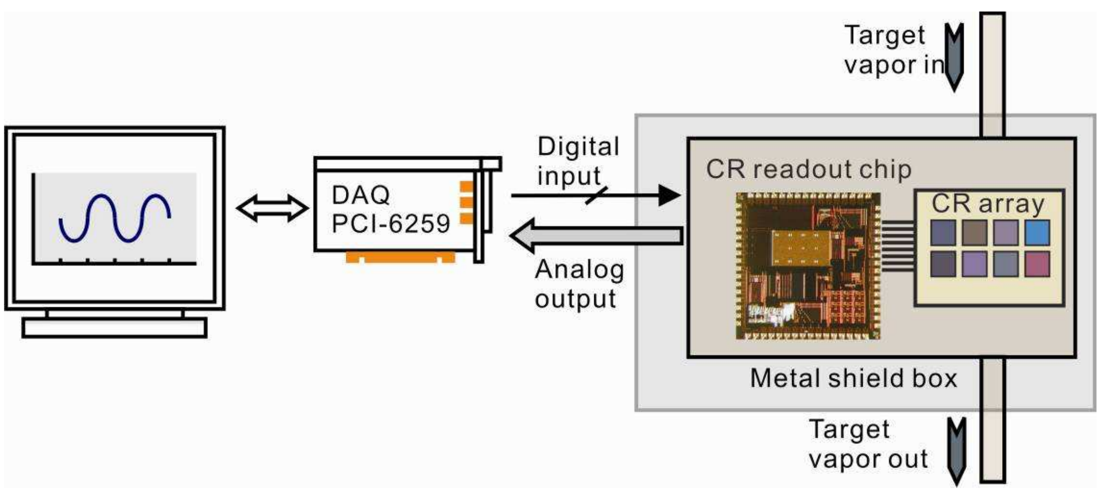

Figure 4.6. CR sensor array experiment setup diagram.

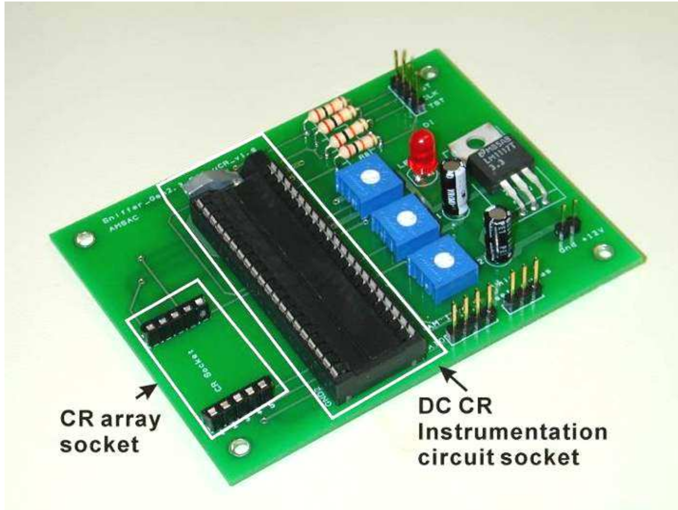

Figure 4.7. Photo of the customized PCB for interfacing a CR-sensor array to the CR instrumentation chip.

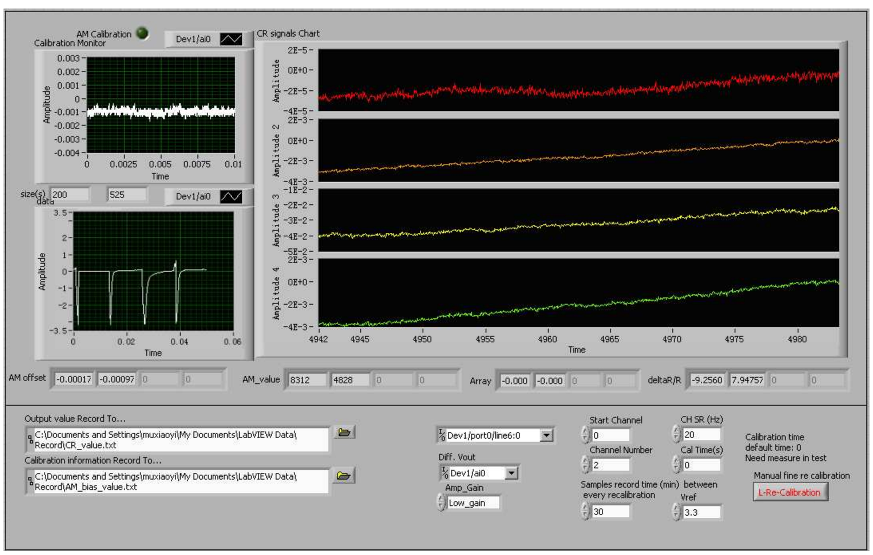

Figure 4.8. LabVIEW graphic user interface for CR sensor array test, providing a customized setup and a virtual oscilloscope.

4.3.2 Baseline cancellation verification

To verify baseline cancellation function of the DC CR instrumentation circuit, a test was performed using the experiment setup described in section 4.3.1. The DC CR instrumentation circuit was used to record outputs from OPH-MPN CR array. Figure 4.9. shows OPH-MPN CR sensor response to 2-butanone at room temperature and the corresponding output of CR instrumentation circuit. Different concentration of 2-butanone were dosed in each dosing phase. The CR had a slight resistance response at dosing phase and is recovered back to baseline value at recovering phase. The circuit was calibrated at the start of the first dose, sampled the baseline value and output the amplified baseline-cancelled response. Performing baseline cancellation, the CR instrumentation chip dramatically amplifies the resistance change as a result.

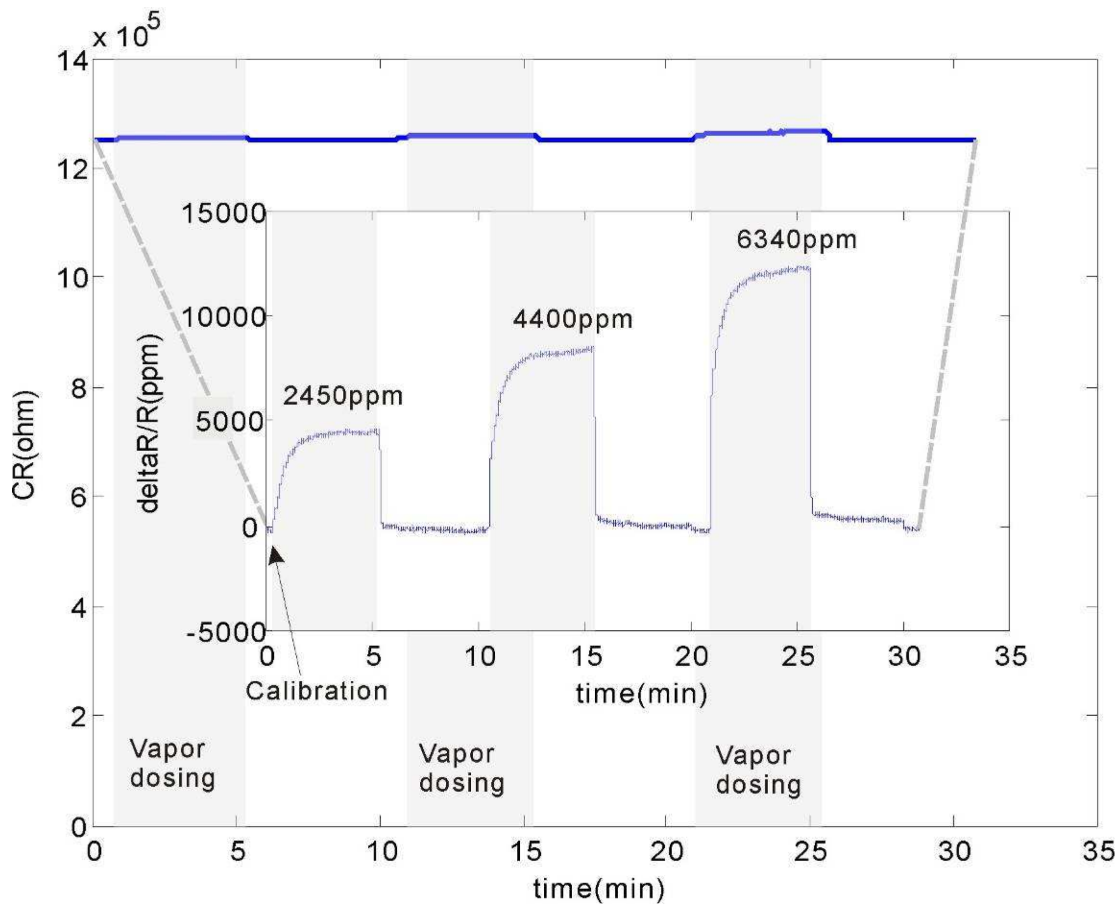

Figure 4.9. OPH-MPN-CR sensor responding to 2-butanone at room temperature and corresponding output of CR instrumentation circuit for the sensor response.

4.3.3 Drifting tracking verification

The OPH-MPN CR sensor drifts obviously at higher temperature. To demonstrate the DC CR instrumentation circuit's ability of drift tracking, the chamber was placed in water at temperature 45˚C. Figure 4.10. shows the output of CR instrumentation circuit for OPH-MPN CR sensor responses to 2-butanone at temperature 45˚C. The CR instrumentation circuit calibrates periodically (every 10 minutes) and adjusts the baseline back to zero before the next vapor dosing phase, correcting the error introduced by baseline drifting. The drift observed at the circuit output is larger than minimum response measured. Thus without drift tracking, this variation would add significant error to the measurement.

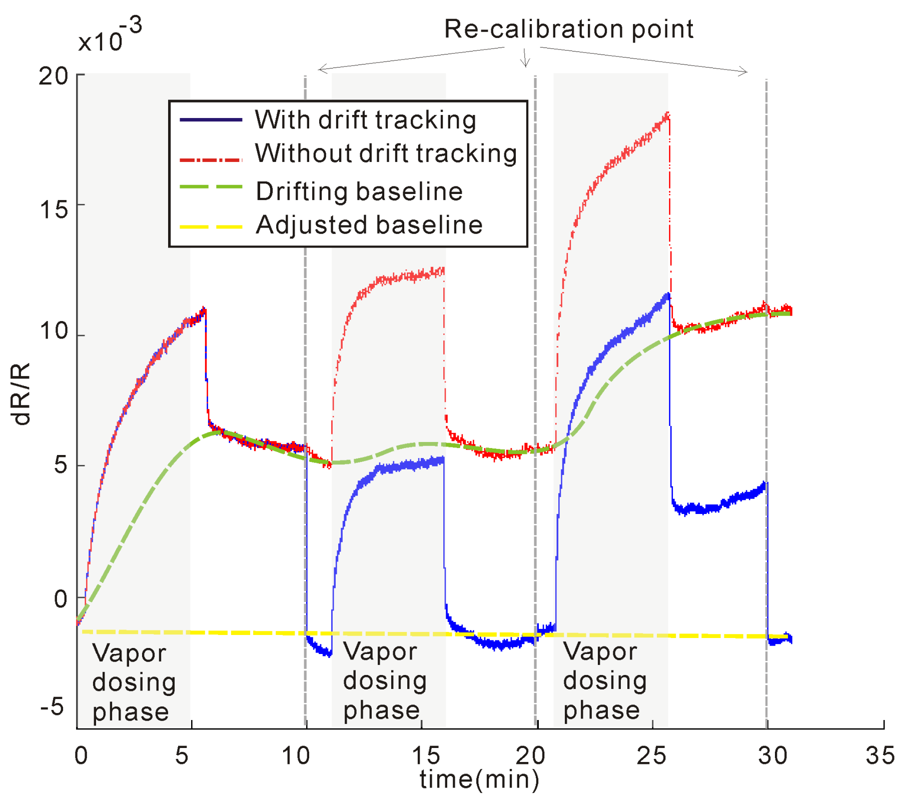

Figure 4.10. Output of CR instrumentation circuit for OPH-MPN CR sensor responses to 2-butanone at temperature 45˚C.

4.3.4 Multiple-channel supporting verification

To demonstrate DC CR instrumentation circuit's ability of the multi-channel supporting, 2-channel OPH-MPN CR array was tested in 2-butanone at room temperature and response was recorded by the DC CR instrumentation circuit. The CR array contains two CR sensors with baseline values of 0.91MΩ and 1.25MΩ and both of them are in the circuit's readout range. Figure 4.11. shows output of 2-channel-CR instrumentation circuit for this CR array response. The CR instrumentation chip performs multi-channel readout and outputs results at 20Hz sampling rate in each channel.

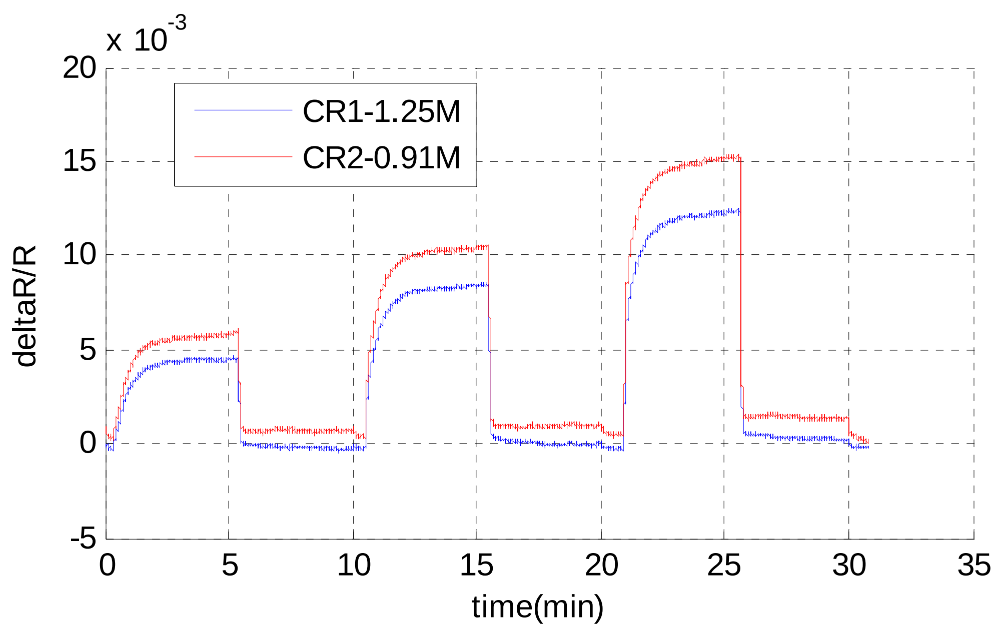

Figure 4.11. Output of 2-channel-CR readout circuit for OPH-MPN CR sensor responses to 2-butanone at room temperature. The CR readout chip performs multi-channel readout and outputs results at 20Hz sampling rate in each channel.

4.3.5 Linearity characterization

To characterize the linearity of the CR instrumentation circuit, the circuit recorded response from OPH-MPN-coated CR sensor with toluene and 2-butanone. Figure 4.12 shows the measured results for ΔR/R as function of test vapor concentration, which represent the calibration curves of the sensor. The output of the system is observed to be good linearity, with R^2 value of 0.998 in toluene and 0.997 in 2-butanone.

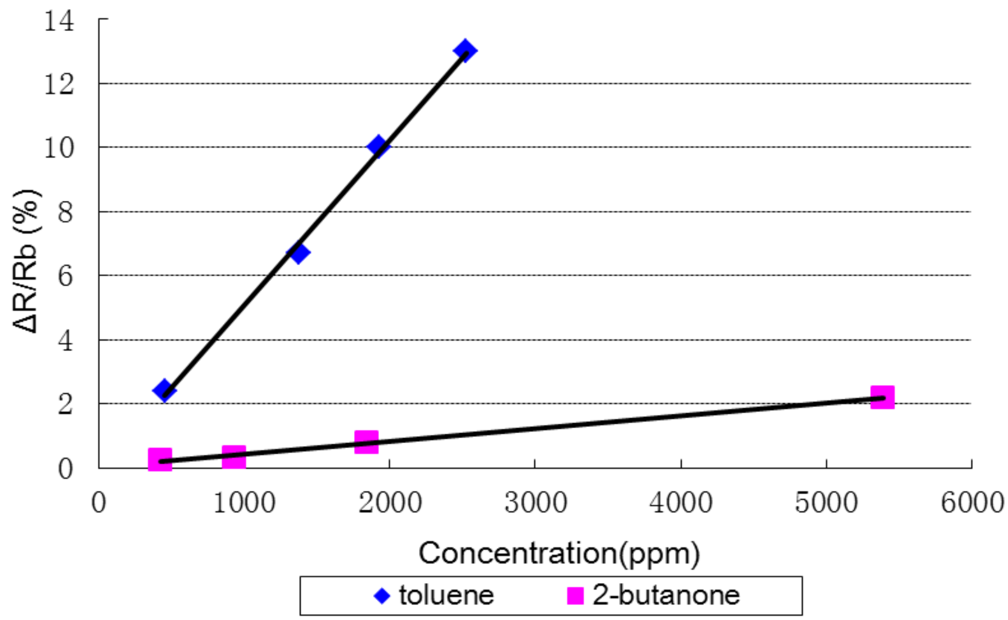

Figure 4.12. Toluene and 2-butanone vapor calibration curves for an OPH-MPN CR.

4.4 Performance summary

In this chapter, the silicon realization of CR instrumentation circuit was characterized and verified by a series of experiments. CR array experiments demonstrated the ability of baseline cancellation, drift tracking and multi-channel supporting, and characterized the linearity of the circuit. Table 4.3 lists all the key performances. In all, this circuit overcomes many of the instrumentation challenges presented by CR sensors, meets the design goals listed in Chapter1 (except resolution) and is well suitable for on-chip sensor array readout.

Process	0.5μm
Power supply	3.3V
Power per channel	66μW
Channel	8
Sampling rate	20Hz
Readout range of ΔR/R(+/-)	12.6%
Rb cancellation range	60kΩ - 10MΩ
ΔR/R resolution	60ppm – 125ppm

Table 4.3. Performance summary of CR DC instrumentation circuit.

5 AC Chemiresistor Instrumentation Circuit Design

In the previous chapter, the silicon realization of the DC CR instrumentation circuit was characterized and verified by a series of experiments. However, the achieved performance in terms of resolution did not meet the target goal of 1ppm. In addition, the MPN-CR device exhibits a capacitance response that is attractive to potentially provide an orthogonal means of vapor measurement. In this chapter, the limitation of the DC approach is first analyzed. Then an alternative solution using AC measurement is presented to overcome the challenge and provide supplemental functionality of capacitance change readout. A circuit designed to implement this approach will be introduced and simulation results will be shown.

5.1 Limitation of DC CR instrumentation circuit

In order to analyze the DC instrumentation circuit's intrinsic noise, excluding CR, a standard carbon film resistor, which has much lower noise than either a CR or the readout circuit, is used in place of the CR. Using a fixed carbon resistor, the DC readout circuit was tested and the equivalent input V_{rms} is noise was found to be 12μV when 1V is applied to a 1Mohm resistor. A simplified noise analysis circuit is given in Figure 5.1 which identifies noise sources including: current bias noise V_{curN}, resistor's intrinsic noise V_{rN}, AM DAC noise V_{dacN}, gain block noise V_{ampN} and power supply's noise V_{regN}. Noise from the power supply, a 3.3V voltage regulator, and AM DAC, a commercial component, were determined from data sheets, and noise levels from the gain block and the current bias and resistor were estimated from simulation. The noise value of each component is listed in Table 5.1. The total estimated noise based on simulation and datasheet is

$$V_{noise\_all} = \sqrt{V_{regN}^{\;2} + V_{dacN}^{\;2} + (V_{curN}^{\;2} + V_{rN}^{\;2}) + V_{ampN}^{\;2}} = 17.7(\mu V) \tag{5.1}$$

which is close to the test result of 12μV. Table 5.1 shows the main noise contribution comes from the current bias. Based on the analysis in Chapter 3, 1/f noise dominants over other sources because the whole system runs at low frequency (20Hz). Although the current bias was designed with large area to minimize 1/f noise, due to area constraints, it cannot be designed large enough to push 1/f noise down to the ppm level. Thus, the DC current source is the main limitation to resolution of the DC readout approach.

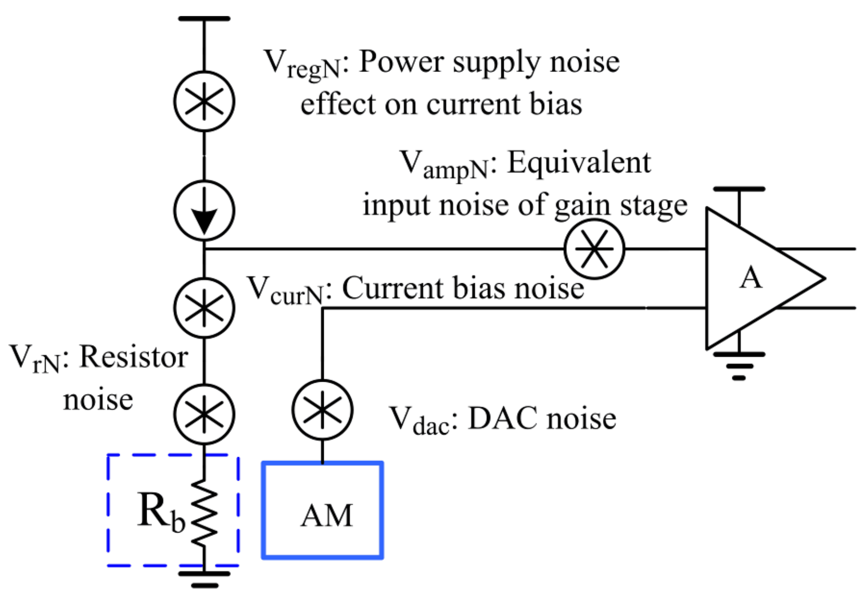

Figure 5.1. Noise analysis circuit of CR instrumentation circuit.

Noise source	Value
V_{regN}	2μV
V_{dacN}	70nV
V_{curN} and V_{rN}	17.6μV
V_{ampN}	0.725μV

Table 5.1. Noise value of each component in noise analysis circuit

5.2 AC CR instrumentation circuit design

To overcome the limitation of DC instrumentation and incorporate information within the sensor's capacitance response, an AC method for measuring impedance is preferable. Building on past work in our lab, an impedance measurement with baseline cancellation (IMBC) technique [65] was chosen as the starting point and adapted to the specifications of MPN-CR sensor arrays. The following sub-sections will first introduce the IMBC algorithm, then present the new AC CR instrumentation circuit implementation. The simulation results are presented and discussed in the last section.

5.2.1 IMBC algorithm

Based on experimental observations, an MPN-CR can be modeled by a resistance and capacitance in parallel as shown in Figure 5.2, where R_b and C_b are baseline values and ΔR and ΔC are sensor response. The goal of the IMBC algorithm is to extract $\Delta R/ R_b$ and $\Delta C/ C_b$ with high resolution. Similar to the DC baseline cancellation procedure, the IMBC system shown in Figure 5.3. extracts baseline R_b and C_b during idle phase and extracts baseline cancelled response ΔR and ΔC during response phase. Four working phases are introduced to extract information by manipulating S1 and S2, which is listed in Table 5.2. The working principle will be presented below.

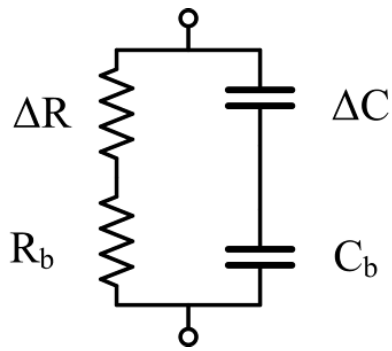

Figure 5.2. Equivalent circuit model of MPN-CR.

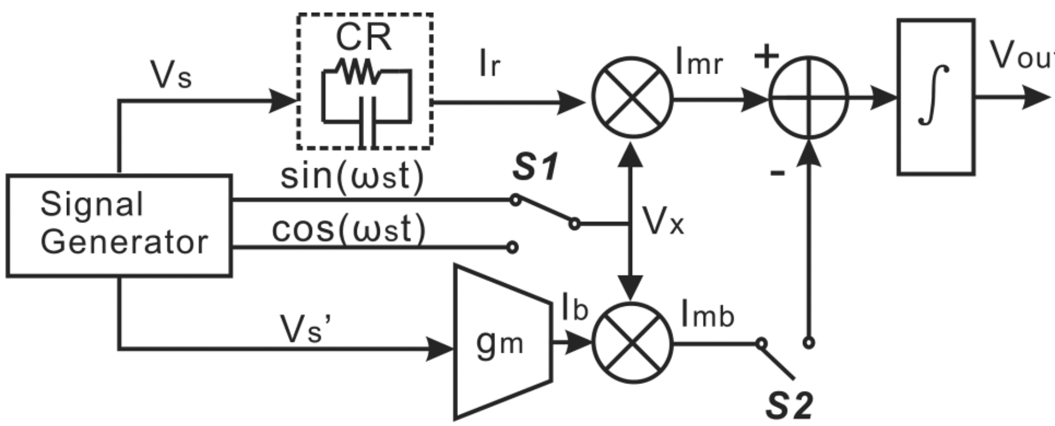

Figure 5.3. IMBC system diagram.

IMBC Phase	CR Phase	S1	S2	Purpose
$Ph_{0,0}$	Idle	sin(ωst)	Off	Extract Rb
$Ph_{0,1}$	Response	sin(ωst)	On	Extract ΔR
$Ph_{1,0}$	Idle	cos(ωst)	Off	Extract Cb
$Ph_{1,1}$	Response	cos(ωst)	On	Extract ΔC

Table 5.2. Four working phases of IMBC system.

CR is stimulated by a sinusoid voltage waveform generator given by

$$V_s(t) = A_s \sin(\omega_s t) \tag{5.2}$$

where A_S is stimulus amplitude and ω_S is stimulus frequency.

The CR's current response to V_S is given by

$$I_r(t) = A_s \,|Y_{CR}|\sin(\omega_s t + \angle Y_{CR}) \tag{5.3}$$

where $|Y_{CR}|$ is the amplitude of CR admittance Y_{CR} and $\angle Y_{CR}$ is the phase of CR admittance Y_{CR}.

In $Ph_{0,0}$, ΔR and ΔC are equal to 0. $I_r(t)$ is multiplied with $\sin(\omega_S t)$ and integrated in one period of $T=2\pi/\omega_S$. the output voltage is obtained by

$$V_{out(0,0)} = \frac{TA_s}{2C_{\text{int}}}\left(\frac{1}{R_b}\right) \tag{5.4}$$

where C_{int} is the integrator capacitance. (Details of derivation will be provided in Appendix A)

Equation (5.4) indicates that the output voltage $V_{out(0,0)}$ during $Ph_{0,0}$ is proportional to $1/ R_b$.

In $Ph_{0,1}$, ΔR and ΔC have values based on the sensor response. To mimic the baseline value of CR, V_s' is generated by the sinusoid voltage waveform generator given by

$$V_s'(t) = A_s \sin(\omega_s t + \angle Y_{CR\_b}) \tag{5.5}$$

And g_m (which can be implemented by operational transconductance amplifier) is adjusted to equal to 1/ $|Y_{CR\_b}|$. The OTA's output I_b is multiplied with $\sin(\omega_s t)$ to obtain I_{mb}. Then the difference between I_{mb} and I_{mr} is integrated in one period $T=2\pi/\omega_s$ and the output voltage is given by

$$V_{out(0,1)} = \frac{TA_s}{2C_{\text{int}}} \frac{\Delta R}{(R_b + \Delta R)R_b} \approx \frac{TA_s}{2C_{\text{int}} R_b{}^2} \Delta R \qquad when \quad \Delta R << R_b \tag{5.6}$$

(Details of derivation will be provided in Appendix A)

Equation (5.6) indicates that the output voltage $V_{out(0,1)}$ during $Ph_{0,1}$ is proportional to $\Delta R / R_b{}^2$.

Dividing (5.6) by (5.4), $\Delta R / R_b$ is acquired by

$$\frac{\Delta R}{R_b} = -\frac{V_{out(0,1)}}{V_{out(0,0)}} \tag{5.7}$$

Similarly, when applying cosine waveform $\cos(\omega_s t)$ in $Ph_{1,0}$ and $Ph_{1,1}$, the outputs are given by

$$V_{out(1,0)} = \frac{TA_s}{2C_{\text{int}}} \omega_s C_b \tag{5.8}$$

$$V_{out(1,1)} = \frac{TA_s}{2C_{\text{int}}} \omega_s \Delta C \tag{5.9}$$

(Details of derivation will be provided in Appendix A)

Dividing (5.9) by (5.8), $\Delta R/ R_b$ is acquired by

$$\frac{\Delta C}{C_b} = \frac{V_{out(1,1)}}{V_{out(1,0)}} \tag{5.10}$$

Thus both $\Delta R/ R_b$ and $\Delta C/ C_b$ are successfully extracted by IMBC algorithm.

Notice that $V_{out(0,1)} << V_{out(0,0)}$ and $V_{out(1,1)} << V_{out(1,1)}$ because $\Delta R << R_b$ and $\Delta C << C_b$. To digitize $V_{out(0,1)}$ and $V_{out(1,1)}$ with maximum resolution, variable gain is preferable in the IMBC system. By providing programmable gain Ai in I_r and I_b, programmable integrator capacitance C_{int}, and variable integrating time (N periods of T), V_{out} in $Ph_{0,1}$ and $Ph_{1,1}$ can be amplified to the same amplitude level as in $Ph_{0,0}$ and $Ph_{0,1}$. Annotating Ai, C_{int} and N with index (n1,n2), which corresponds four IMBC system phases, Equation (5.4), (5.6)~(5.10) can be rewritten as follows:

$$V_{out(0,0)} = \frac{Ai_{(0,0)} N_{(0,0)} TA_s}{2C_{\text{int}(0,0)}} \left(\frac{1}{R_b}\right) \tag{5.11}$$

$$V_{out(0,1)} = \frac{Ai_{(0,1)} N_{(0,1)} TA_s}{2C_{\text{int}(0,1)} R_b{}^2} \Delta R \tag{5.12}$$

$$\frac{\Delta R}{R_b} = -\frac{V_{out(0,1)}}{V_{out(0,0)}} \cdot \frac{Ai_{(0,1)}}{Ai_{(0,0)}} \frac{C_{\mathrm{int}(0,0)}}{C_{\mathrm{int}(0,1)}} \cdot \frac{N_{(0,1)}}{N_{(0,0)}} \tag{5.13}$$

$$V_{out(1,0)} = \frac{Ai_{(1,0)} N_{(1,0)} T A_s}{2C_{\mathrm{int}(1,0)}} \omega_s C_b \tag{5.14}$$

$$V_{out(1,1)} = \frac{Ai_{(1,1)} N_{(1,1)} T A_s}{2C_{\mathrm{int}(1,1)}} \omega_s \Delta C \tag{5.15}$$

$$\frac{\Delta C}{C_b} = \frac{V_{out(1,1)}}{V_{out(1,0)}} \cdot \frac{Ai_{(1,1)}}{Ai_{(1,0)}} \frac{C_{\mathrm{int}(1,0)}}{C_{\mathrm{int}(1,1)}} \cdot \frac{N_{(1,1)}}{N_{(1,0)}} \tag{5.16}$$

Equation (5.13) shows that $\Delta R / R_b$ is independent of stimulus frequency ω_s. Thus with a high frequency AC stimulus, the system can avoid 1/f noise. With the variable gains, maximum resolution will be utilized when digitizing V_{out} in each IMBC phase, thus improving resolution of $\Delta R / R_b$ and $\Delta C / C_b$.

5.2.2 Circuit implementation

The functionality of Figure 5.3 IMBC algorithm can be realized by several analog circuit blocks which include an amperometry, an OTA, two chopper multipliers, and a ΣΔ ADC. As described below, each of these blocks were designed to minimize complexity while achieving AC instrumentation circuit’s requirements.

5.2.2.1 Amperometry

To readout CR current response I_r due to the AC voltage stimulus V_s, an amperometry is required. Programmable gain is essential to amplify I_r with different magnitudes during different phases. The amperometry with programmable gain adapted from [65] was shown in Figure 5.4. The closed-loop opamp was used to clamp CR between AC voltage source and DC ground and introduce I_r into the current mirror block. I_B is the bias current in the mirror block to set the operational point. By duplicating current mirror A times, and using multiplexer to select the amount of branches, a programmable gain from 5 to 200 was realized. The current mirror was design as cascade structure to minimize the current mirror error.

5.2.2.2 Operational transconductance amplifier

To reproduce the baseline value during the CR response phase, an operational transconductance amplifier (OTA) with variable g_m is required. The g_m needs to be adjusted to 1/ $|Y_{CR\_b}|$. $|Y_{CR\_b}|$ is from 100kΩ to 10MΩ, thus g_m is expected to range from 100nS to 10uS. The OTA was implemented [65] as shown in Figure 5.5. with g_m=1/R_{dsMr}. By tuning the gate voltage of Mr V_r, g_m can be adjusted to the required range. Because Mr is working in the linear region, g_m is linear with V_r. M3 and M4 is designed to attenuate ΔVi, keeping Mr in the linear region.

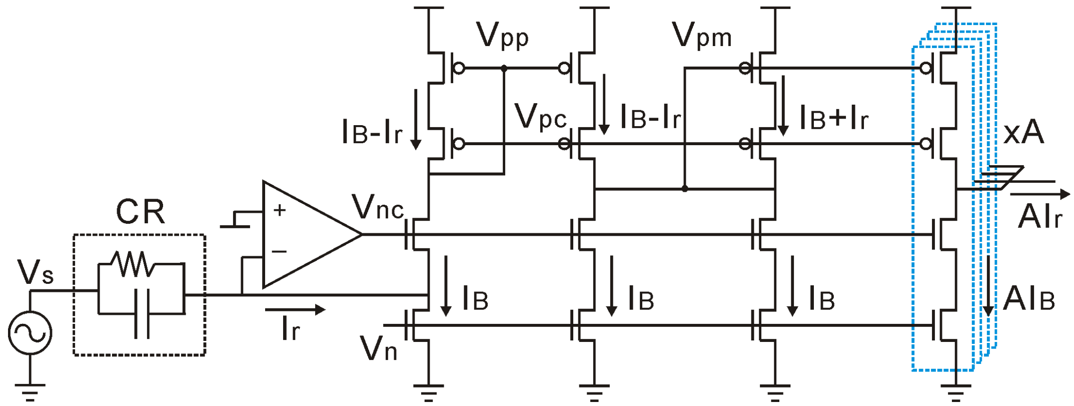

Figure 5.4. Schematic of amperometry circuit in AC instrumentation circuit. The amperometry is designed to readout the CR current response, and provide programmable gain.

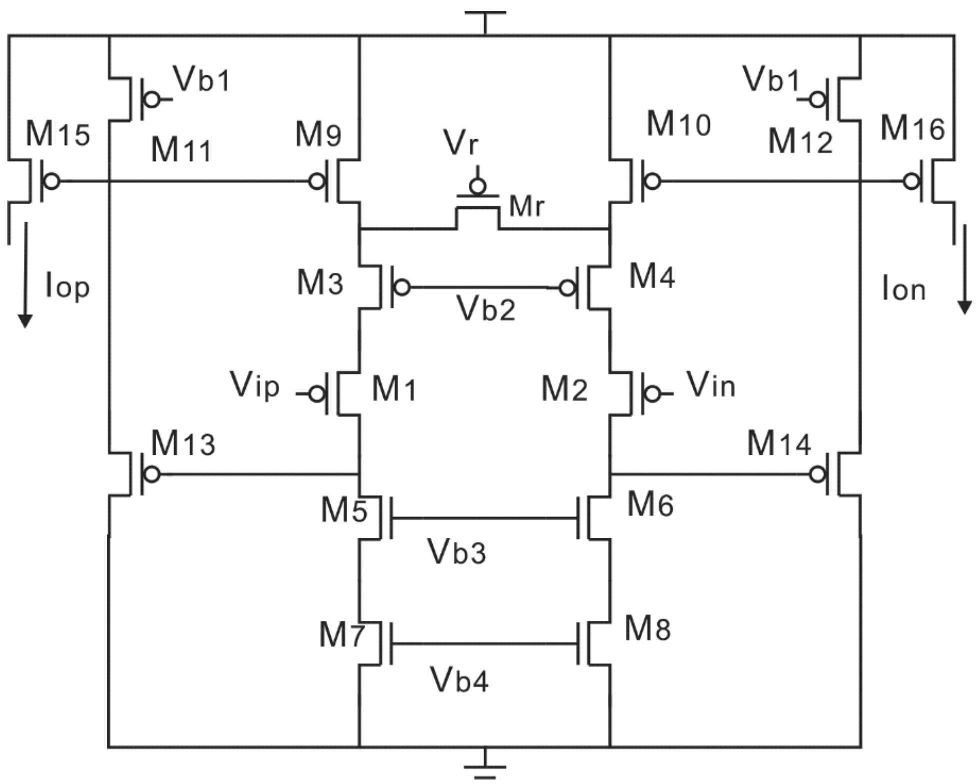

Figure 5.5. Schematic of OTA in AC instrumentation circuit. The OTA reproduces the baseline value during the CR response phase.

5.2.2.3 Chopper multiplier

The multiplication functions in Figure 5.3 can be realized by a circuit that implements the chopping technique [66]. A chopper circuit has been shown to be the best choice for a multiplier in an AC response analyzer because it minimizes complexity while achieving performance goals [67]. The undesirable harmonics generated by the chopper function will be suppressed in the integrator function that follows multiplication in the Figure 5.3.

Two multiplier needs to be realized in AC instrumentation circuit as shown in Figure 5.3. Observing that the amperometry in Figure 5.4. has current branches with current flow I_B-I_r and I_B+I_r, it is readily to flip the direction of the output current by alternately mirroring these two current branches. In this manner, the multiplier after amperometry is able to be incorporated into the amperometry as shown in Figure 5.6. The designed OTA inherently provides differential output, thus the chopper multiplier after the OTA can be implemented by multiplexer as shown in Figure 5.7.

5.2.2.4 Sigma-delta ADC

The integration function of the IMBC algorithm is implemented using a ΣΔ ADC. The ΣΔ ADC provides the added benefits of digitizing the output signal while also reducing low frequency noise. The current mode ΣΔ ADC[65] shown in Figure 5.8 uses a switched capacitor approach to implement the Δ function and eliminate the mismatch problem in traditional (up-down current bias) current mode ΣΔ ADC. A compact dual-level amplifier-based comparator [67] is utilized, outputs +1 when $V_{amp} > V_{th}$, and -1 when $V_{amp} <- V_{th}$. The counter counts up or down based on the comparator's output polarity. According to the different value of the comparator's output, the digital control block manipulates φ1 and φ2 as shown in Figure 5.8., which determines charge/discharge on C_{int}. With oversampling rate of 128, the first-order ΣΔ ADC can achieve 10-bit resolution.

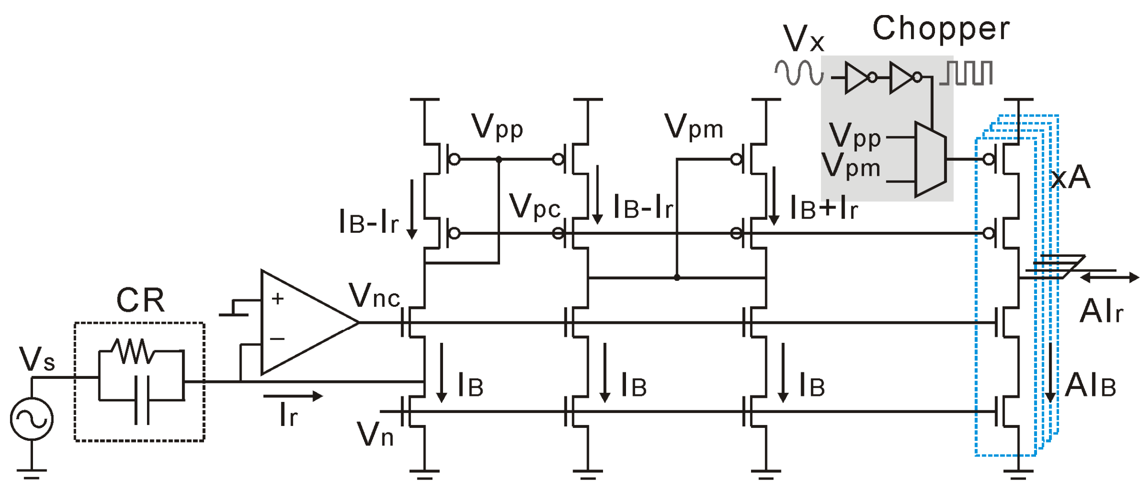

Figure 5.6. Schematic of amperometry circuit incorporating chopper multiplier.

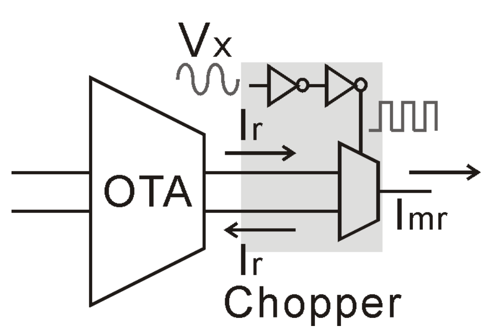

Figure 5.7. Schematic of chopper multiplier and OTA in AC instrumentation circuit.

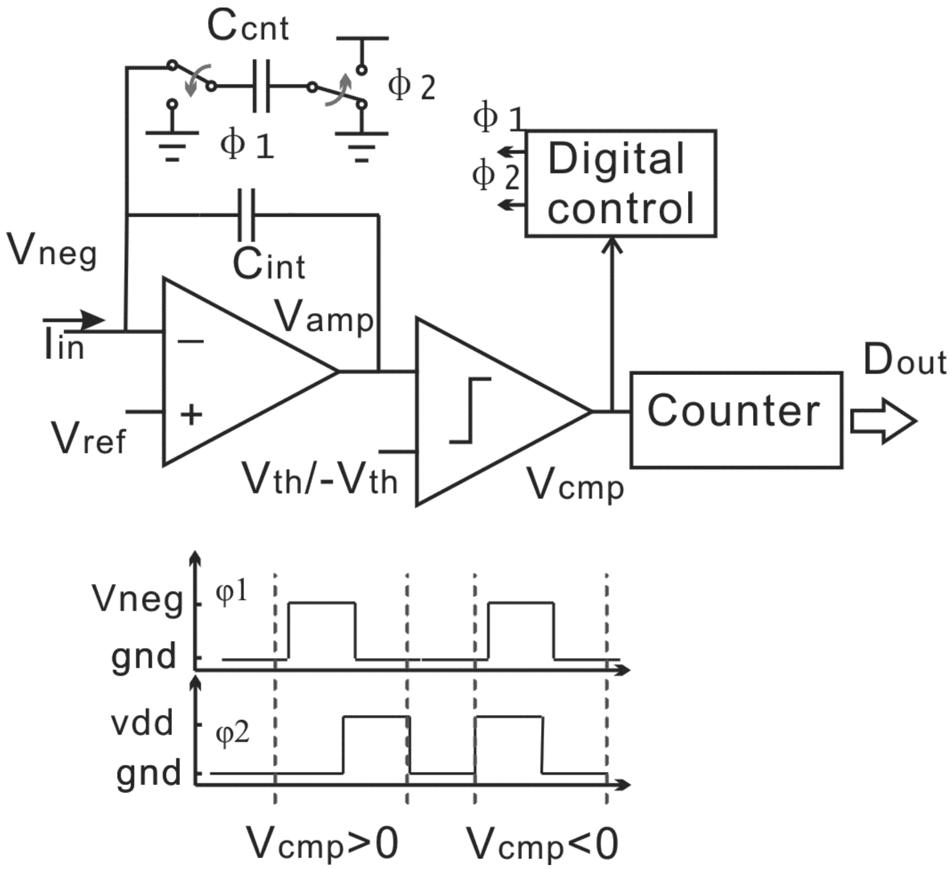

Figure 5.8. Schematic of ΣΔ ADC and timing chart of φ1 and φ2.

5.3 AC CR instrumentation results

In this section, simulation will be given to demonstrate the functionality of IMBC. The AC CR instrumentation circuit was implemented with programmable amperometry gain Ai ranging from x5 to x200, a programmable integrator capacitor C_{int} ranges from 6.4pF to 400fF. In the CR idle phase, a small mirror gain and large capacitor are selected to ensure V_{out} does not exceed the output range. In the CR response phase, the baseline generator is activated and only the response current is fed into the integrator. To increase the resolution, a high gain and small capacitor value would be selected and more than one integration cycle would be run to amplify the small baseline-cancelled signal.

The simulation runs all the four phases of IMBC. Figure 5.9 shows the simulated output plots of the circuit measuring a 0.1% change from a 1MΩ baseline R_b with 10kHz sinusoid stimulus. The ΣΔ ADC oversampling rate is 250. x5 mirror gain and 6.4pF integrator capacitor were chosen in $Ph_{0,0}$ and x40 mirror gain and 400fF integrator capacitor were chosen in $Ph_{0,1}$. Figure 5.8 shows both the integrator output and the comparator output in $Ph_{0,0}$ and $Ph_{0,1}$. The comparator detects whether the output of integrator exceeds the Vth or –Vth, and output 1/-1 correspondingly. The counter output value is 14 in $Ph_{0,0}$ after 1 integration cycle and -16 in $Ph_{0,1}$ after 10 cycles. $\Delta R/R_b$ can be calculated by Equation (5.15), which is 0.102%. The readout only has 20ppm error. Figure 5.10 shows simulated waveform plots of circuit extracting 10% change of a 1pF baseline C_b with 10kHz sinusoid waveform. All the setups are similar to the one in R_b addressing. The counter outputs 1 in $Ph_{1,0}$ phase (1 cycle) and 10 in $Ph_{1,1}$ (10 cycles). $\Delta C/C_b$ can be calculated by Equation (5.18), which is 0.89%. The readout has 0.11% error.

To characterize the resolution of AC instrumentation circuit, ΔR/R was swept from 1 to 100ppm in a 100kΩ R_b. The quantization noise of IMBC was characterized, as shown in Figure 5.11. The maximum noise in this range is 1.22ppm, which is equivalent to the best resolution of 1.22ppm.

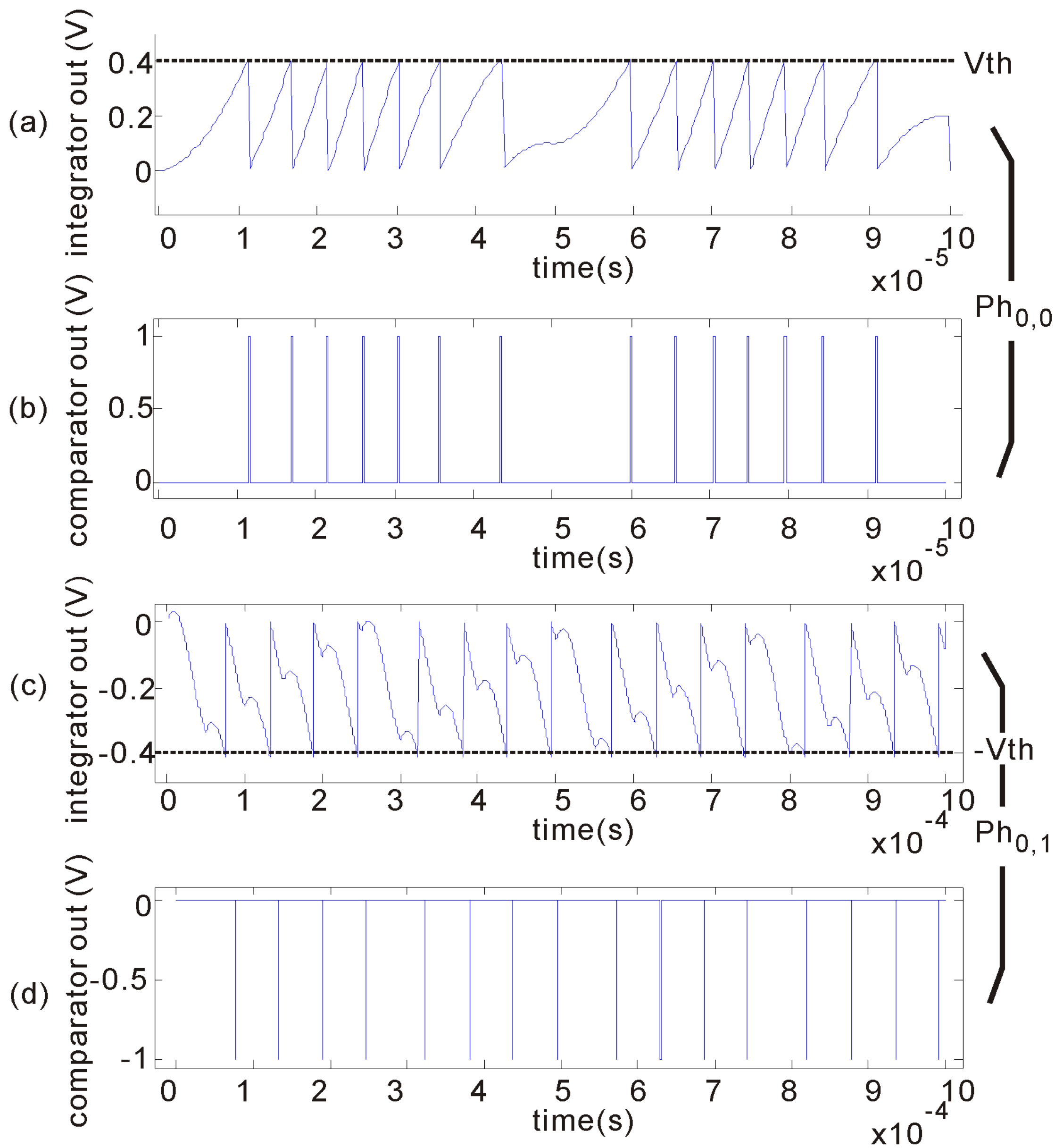

Figure 5.9. Simulated waveform plots of circuit extracting 0.1% change of 1MΩ R_b with 10kHz sinusoid stimulus. (a) The integrator output during $Ph_{0,0}$; (b) The comparator output during $Ph_{0,0}$; (c) The integrator output during $Ph_{0,1}$; (d) The comparator output during $Ph_{0,1}$.

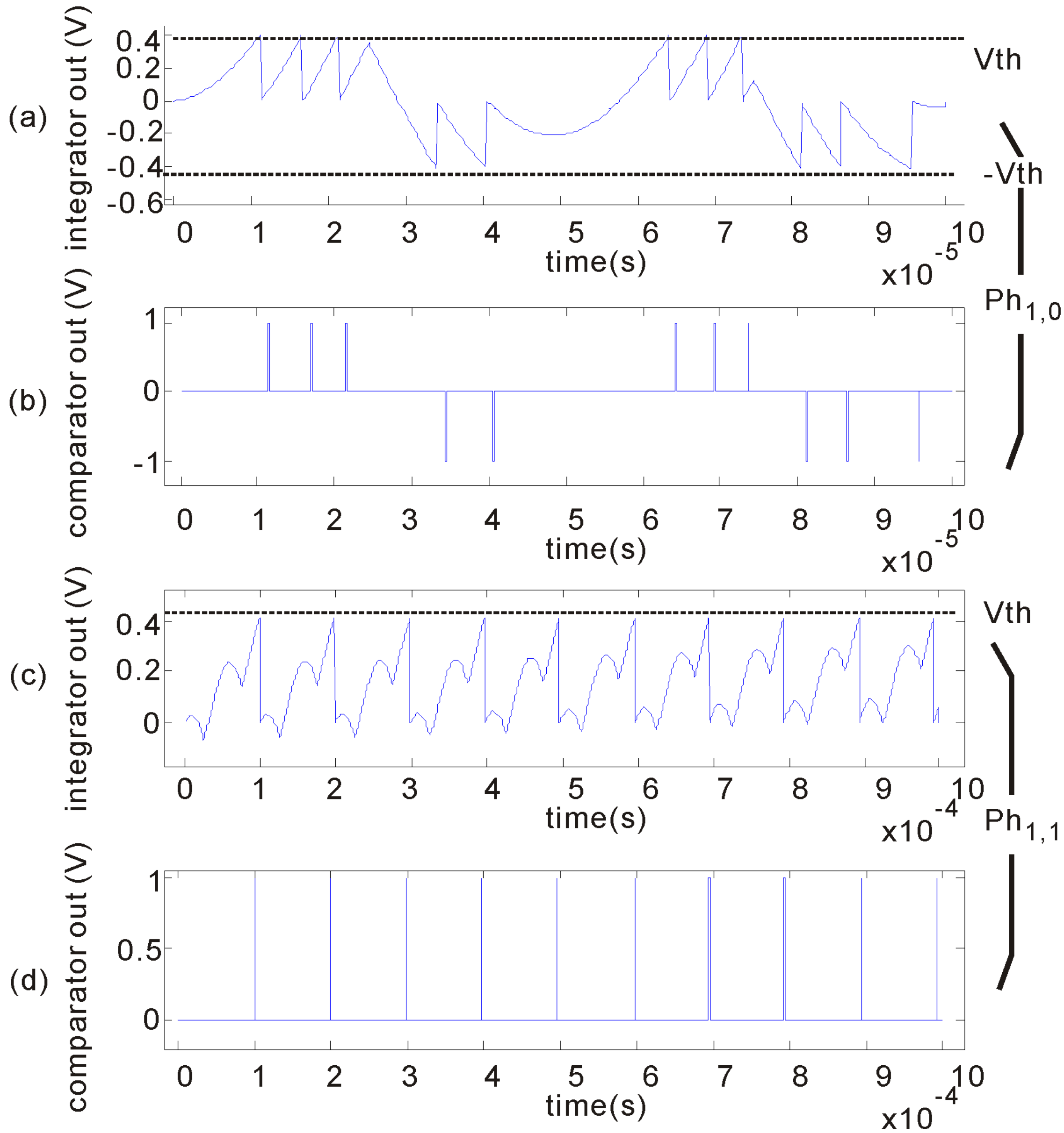

Figure 5.10. Simulated waveform plots of circuit extracting 1% change of 1pF C_b with 10kHz sinusoid stimulus. (a) The integrator output during $Ph_{1,0}$; (b) The comparator output during $Ph_{1,0}$; (c) The integrator output during $Ph_{1,1}$; (d) The comparator output during $Ph_{1,1}$.

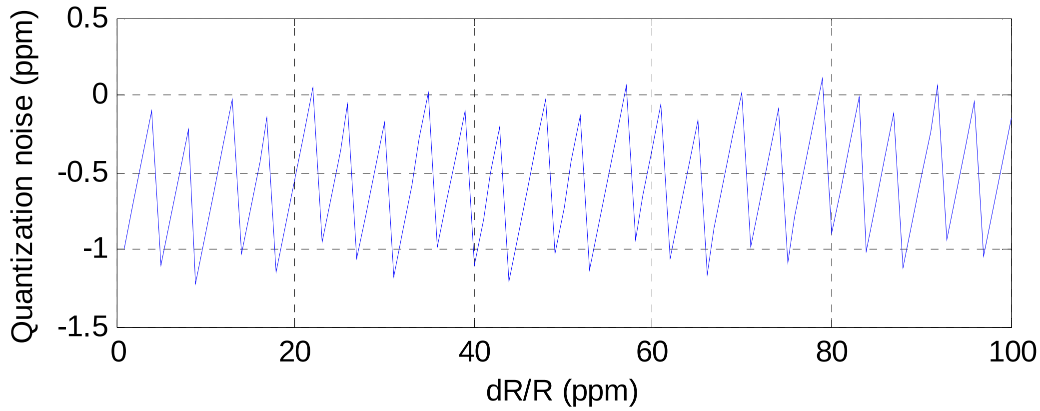

Figure 5.11. Simulated quantization noise for AC instrumentation circuit demonstrates a resolution of 1.22ppm is achieved.

5.4 Discussion

The IMBC algorithm was proved by the simulation results. The baseline-cancelled responses are magnified by mirror gain, integrator capacitance and integration time, which provide a similar level of the digital output to the baseline. Recalling Chapter 3, baseline cancellation and amplification is able to contribute extra $\log_2(A)$ bits resolution compared to direct linear conversion. However, a very large gain could deteriorate the linearity and accuracy due to mismatch, which limits the resolution boost. In AC instrumentation circuit, because there are three tunable gain-parameters, the total gain A can be designed very large while each gain part still keeps small mismatch and total measurement time is short. By adjusting ratio of mirror gain, integrator capacitance and integration period between ideal phase and response phase, ultra-high resolution is achievable. As shown in Figure 5.10., setting Ai ratio equal to 20, C_{int} ratio equal to 16, N ratio equal to 20 and choose oversampling rate as 250, the system reaches 1.22ppm resolution in terms of quantization noise. The 1/f noise, which is an obstacle to achieve high resolution in DC CR instrumentation circuit, can be omitted because the whole system is running at high frequency and ΣΔ modulation further helps to reduce noise.

6 Summary and Future Work

6.1 Summary of the contributions

The μGC is a promising vapor analysis tool for environmental monitoring, military detection, healthcare diagnosis, and many new applications that can benefit from small size, low cost, and high sensitivity. The significance of the μGCs and the instrumentation requirements for MPN-CR arrays (as μGC detectors) were discussed, and existing CR readout technologies were reviewed. A new DC CR instrumentation circuit with high sensitivity and wide dynamic range was introduced. Based on the test results and analysis of the DC circuit, a new AC CR instrumentation circuit with ultra high resolution was presented. In addition, a methodology for integrating CR arrays directly onto the surface of the instrumentation chip was described. The results of this research address the instrumentation challenges in high sensitivity μGCs. The main contributions in this research are described below.

Contribution 1: Developed a new DC instrumentation circuit that overcomes the unique performance limitations of MPN-coated CR sensors.

MPN-CR sensors show great promise in achieving the high resolution requirement of μGCs but suffer from a key challenge due to their large baseline values (relative to their response signal) that vary unpredictably from device to device. Compared to any reported resistive readout circuits, the DC instrumentation circuit introduced in this thesis achieves the best resolution ($\Delta R/R_b$ better than 125ppm) over the 60k to 10MΩ baseline range (see Table 4.2). This performance is equivalent to a 120dB dynamic range. The DC chip provides eight sensor readout channels, consumes only 66μW per channel and ideally suited for μGCs featuring MPN-CR sensor arrays.

Contribution 2: Implemented the first ever CMOS instrumentation circuit with an MPN-coated CR array on the chip's surface.

Integrating the CR array on the readout chip's surface is an important step in minimizing μGC size. It also improves sensitivity by eliminating environmental noise. The key challenge is establishing a methodology that provides compatibility between CMOS and the MPN coating process. The MPN coating process, developed and carried out by colleagues at The University of Michigan, was thoroughly studied; damage to CMOS circuitry caused by electron-beam patterning and cross-linking was identified. Multiple solutions were explored, and most suitable approach was demonstrated in a prototype CMOS instrumentation circuit with on-chip MPN-CR array. The prototype CMOS MPN-CR array established a platform that is suitable for integration with a microfluidics cap that creates a vapor flow chamber necessary to implement the overall μGC.

Contribution 3: Adapted the AC baseline cancelation readout approach to implement an ultra high resolution CR readout circuit.

The DC instrumentation circuit has a limited resolution due to the flicker noise inherent in the DC stimulus. An AC baseline cancelation readout approach developed for biosensors was adapted to the design requirements of CR sensor arrays. The resulting CMOS circuit demonstrates that the resistance and capacitance of an MPN-coated CR can be extracted with resolution as high as 1.22ppm. This circuit shows strong potential to overcome the resolution limitation of the DC instrumentation circuit.

6.2 Future work

Based on the results of this thesis, the following suggestions for future research are made.

6.2.1 Fully on-chip-CR-array instrumentation system

Fully on-chip-CR-array instrumentation system will be built based on the on-chip-CR-array readout circuit. Figure 6.1. shows an illustration of on-CMOS microsystem concept, integrating a CR array and a microfluidic vapor chamber. Future work with our collaborators will focus on the realization, validation and characterization of the fully-integrated microsystem, which will finally be incorporated into μGC.

6.2.2 Maturation of IMBC algorithm

Preliminary work of IMBC algorithm has been done. Simulation results have been shown to demonstrate the functionality of IMBC and 1st generation of AC CR instrumentation chip based on IMBC algorithm has been fabricated. Future work will focus on the test, verification and characterization of the Gen1 AC chip and based on the analysis of the test results, 2nd generation AC chip will be developed with fully VLSI implementation and on-chip CR array compatibility.

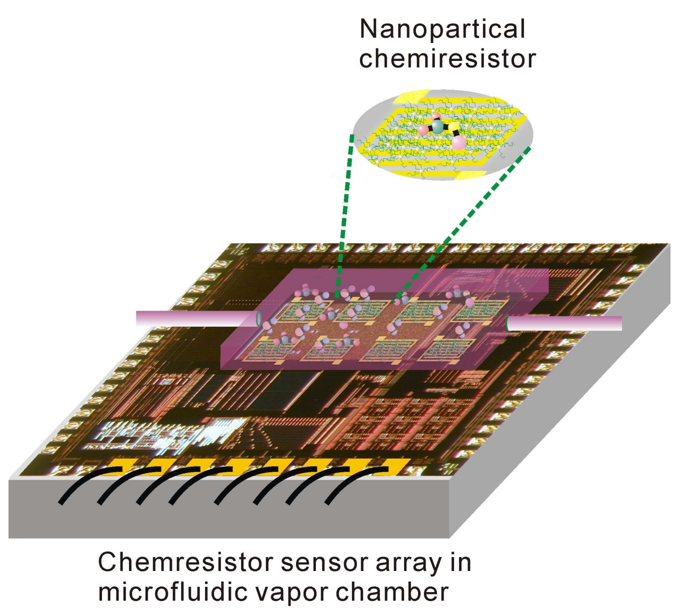

Figure 6.1. Illustration of the micro CR sensor system.

APPENDIX

Appendix A

Derivation of V_{out} in $Ph_{0,0}$

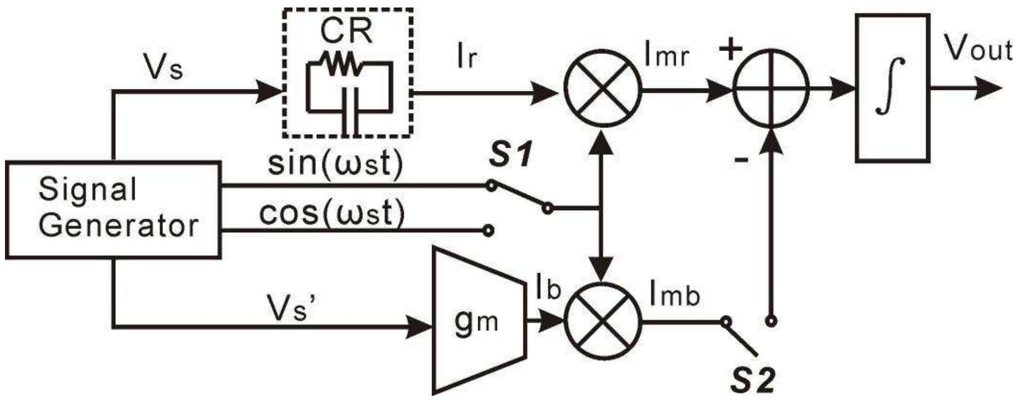

Figure A.1. IMBC system diagram.

The total admittance $Y_{CR}(\omega)$ is given by

$$Y_{CR}(\omega) = \frac{1}{R_b + \Delta R} + j\omega(C_b + \Delta C) \tag{A.1}$$

where ω is the angular frequency. Following the definitions in Chapter 3, ΔR and ΔC are equal to zero in the idle phase, and during response phase, ΔR and ΔC have values based on the sensor response. The baseline admittance in the idle phase is designated by

$$Y_{CR\_b}(\omega) = \frac{1}{R_b} + j\omega(C_b) \tag{A.2}$$

As given in Chapter 5, stimulus voltage is

$$V_s(t) = A_s \sin(\omega_s t) \tag{A.3}$$

The CR's current response to V_S is given by

$$I_r(t) = A_s \, |Y_{CR}| \sin(\omega_s t + \angle Y_{CR}) \tag{A.4}$$

where $|Y_{CR}|$ is the amplitude of CR admittance Y_{CR} and $\angle Y_{CR}$ is the phase of CR admittance Y_{CR}.

$I_r(t)$ is multiplied with $\sin(\omega_s t)$ to acquire $I_{mr}(t)$ which is given by

$$\begin{aligned} I_{mr}(t) &= A_s \, |Y_{CR}| \sin(\omega_s t + \angle Y_{CR}) \sin(\omega_s t) \\ &= \frac{1}{2} A_s \, |Y_{CR}| [-\cos(\angle Y_{CR}) + \cos(2\omega_s t + \angle Y_{CR})] \\ &= -\frac{1}{2}\frac{A_s}{R_b} + \frac{1}{2} A_s \, |Y_{CR}| \cos(2\omega_s t + \angle Y_{CR}) \end{aligned} \tag{A.5}$$

After integration, the output of the integrator is

$$V_{out(0,0)} = \int_0^T \frac{I_{mr}(t)}{C_{\text{int}}} dt \tag{A.6}$$

where C_{int} is the integrator capacitance.

By Substituting (A.5) in (A.6)

$$V_{out(0,0)} = \int_0^T [-\frac{1}{2}\frac{A_s}{R_b} + \frac{1}{2}A_s \,|Y_{CR\_b}|\cos(2\omega_s t + \angle Y_{CR\_b})]/C_{\text{int}}dt$$
$$= -\frac{TA_s}{2C_{\text{int}}} + 0$$
$$= -\frac{TA_s}{2C_{\text{int}}}(\frac{1}{R_b}) \tag{A.7}$$

Thus, Equation (5.4) is approved.

Derivation of V_{out} in $Ph_{0,1}$

In $Ph_{0,1}$, ΔR and ΔC have values based on the sensor response. To mimic the baseline value of CR, V_s' is generated by the sinusoid voltage waveform generator given by

$$V_s'(t) = A_s \sin(\omega_s t + \angle Y_{CR\_b}) \tag{A.8}$$

and OTA's g_m is adjusted to equal to 1/|Y_{CR_b}|. The OTA's output I_b is expressed as

$$I_b(t) = A_s \,|Y_{CR\_b}|\sin(\omega_s t + \angle Y_{CR\_b}) \tag{A.9}$$

I_{mb} is acquired from multiplication of I_b and sin(ω_st), given by

$$I_{mb}(t) = A_s \,|Y_{CR\_b}|\sin(\omega_s t + \angle Y_{CR\_b})\sin(\omega_s t)$$
$$= \frac{1}{2}A_s \,|Y_{CR\_b}|[\cos(2\omega_s t + \angle Y_{CR\_b}) - \cos(\angle Y_{CR\_b})]$$
$$= -\frac{1}{2}A_s \Re(Y_{CR\_b}) + \frac{1}{2}A_s \,|Y_{CR\_b}|\cos(2\omega_s t + \angle Y_{CR\_b}) \tag{A.10}$$

where $\Re(Y_{CR\_b}) = 1/R_b$, is the real part of Y_{CR_b}.

The difference between I_{mb} and I_{mr} is integrated in one period $T=2\pi/\omega_s$ and the output voltage is given by

$$\begin{aligned}
V_{out(0,1)} &= \int_0^T \frac{[I_{mr}(t) - I_{mb}(t)]}{C_{\text{int}}} dt \\
&= \int_0^T \{-\frac{1}{2} A_s \Re(Y_{CR}) + \frac{1}{2} A_s |Y_{CR}| \cos(2\omega_s t + \angle Y_{CR}) \\
&- [-\frac{1}{2} A_s \Re(Y_{CR_b}) + \frac{1}{2} A_s |Y_{CR_b}| \cos(2\omega_s t + \angle Y_{CR_b})]\} / C_{\text{int}} dt \\
&= -\frac{T}{2} A_s \Re(Y_{CR}) / C_{\text{int}} + \frac{T}{2} A_s \Re(Y_{CR_b}) / C_{\text{int}} \\
&= \frac{T}{2} A_s (-\frac{1}{R_b + \Delta R} + \frac{1}{R_b}) / C_{\text{int}} \\
&= \frac{TA_s}{2C_{\text{int}}} \frac{\Delta R}{(R_b + \Delta R) R_b} \\
&\approx \frac{TA_s}{2C_{\text{int}} R_b^2} \Delta R \qquad when \quad \Delta R << R_b
\end{aligned} \tag{A.11}$$

Thus, Equation (5.6) is approved.

Derivation of V_{out} in $Ph_{1,0}$ and $Ph_{1,1}$

Similar to the derivation in Appendix I & II, substituting $\cos(\omega_s t)$ for $\sin(\omega_s t)$ as multiplier input, C_b and ΔC can be extracted in $Ph_{1,0}$ and $Ph_{1,1}$.

In $Ph_{1,0}$,

$$
\begin{aligned}
I_{mr}(t) &= A_s \,|Y_{CR}|\sin(\omega_s t + \angle Y_{CR\_b})\cos(\omega_s t) \\
&= \frac{1}{2} A_s \,|Y_{CR\_b}|[\sin(\angle Y_{CR\_b}) + \sin(2\omega_s t + \angle Y_{CR\_b})] \\
&= \frac{1}{2} A_s \Im(Y_{CR\_b}) + \frac{1}{2} A_s \,|Y_{CR\_b}|\sin(2\omega_s t + \angle Y_{CR\_b})
\end{aligned}
\tag{A.12}
$$

where $\Im(Y_{CR\_b}) = \omega_s C_b$, is the imaginary part of Y_{CR_b}.

$$
\begin{aligned}
V_{out(1,0)} &= \int_0^T \frac{I_{mr}(t)}{C_{\text{int}}} dt \\
&= \int_0^T [\frac{1}{2} A_s \Im(Y_{CR\_b}) - \frac{1}{2} A_s \,|Y_{CR\_b}|\cos(2\omega_s t + \angle Y_{CR\_b})] dt / C_{\text{int}} \\
&= \frac{TA_s}{2C_{\text{int}}} \Im(Y_{CR\_b}) \\
&= \frac{TA_s}{2C_{\text{int}}} \omega_s C_b
\end{aligned}
\tag{A.13}
$$

Thus, Equation (5.8) is approved.

In $Ph_{1,1}$,

$$
\begin{aligned}
I_{mr}(t) &= A_s \,|Y_{CR}|\sin(\omega_s t + \angle Y_{CR})\cos(\omega_s t) \\
&= \frac{1}{2} A_s \,|Y_{CR}|[\sin(\angle Y_{CR}) + \sin(2\omega_s t + \angle Y_{CR})] \\
&= \frac{1}{2} A_s \Im(Y_{CR}) + \frac{1}{2} A_s \,|Y_{CR}|\sin(2\omega_s t + \angle Y_{CR})
\end{aligned}
\tag{A.14}
$$

$$I_{mb}(t) = A_s\,|Y_{CR\_b}|\sin(\omega_s t + \angle Y_{CR\_b})\cos(\omega_s t)$$
$$= \frac{1}{2}A_s\,|Y_{CR\_b}|[\sin(\angle Y_{CR\_b}) + \sin(2\omega_s t + \angle Y_{CR\_b})]$$
$$= \frac{1}{2}A_s\Im(Y_{CR\_b}) + \frac{1}{2}A_s\,|Y_{CR\_b}|\sin(2\omega_s t + \angle Y_{CR\_b}) \tag{A.15}$$

where $\Im(Y_{CR}) = \omega_s(C_b + \Delta C)$, is the imaginary part of Y_{CR}.

$$V_{out(1,1)} = \int_0^T \frac{[I_{mr}(t) - I_{mb}(t)]}{C_{\text{int}}}dt$$
$$= \int_0^T \{\frac{1}{2}A_s\Im(Y_{CR}) + \frac{1}{2}A_s\,|Y_{CR}|\sin(2\omega_s t + \angle Y_{CR})$$
$$-[\frac{1}{2}A_s\Im(Y_{CR\_b}) + \frac{1}{2}A_s\,|Y_{CR\_b}|\sin(2\omega_s t + \angle Y_{CR\_b})]\}/C_{\text{int}}dt$$
$$= \frac{TA_s}{2C_{\text{int}}}\Im(Y_{CR}) - \frac{TA_s}{2C_{\text{int}}}\Im(Y_{CR\_b})$$
$$= \frac{TA_s}{2C_{\text{int}}}(\omega_s(C_b + \Delta C) - \omega_s C_b)$$
$$= \frac{TA_s}{2C_{\text{int}}}\omega_s\Delta C \tag{A.16}$$

Thus, Equation (5.9) is approved.

BIBLIOGRAPHY

Bibliography

[1] http://en.wikipedia.org/wiki/Gas_chromatograph.

[2] C. Lu, W. H. Steinecker, W. Tian, M. C. Oborny, J. M. Nichols, M. Agah, J. A. Potkay, H. K. L. Chan, J. Driscoll, R. D. Sacks, K. D. Wise, S. W. Pang, E. T. Zellers, "First-generation hybrid MEMS gas chromatograph," *Lab Chip*, vol. 5, no. 10, pp. 1123-1131, 2005.

[3] R. Veeneman, "Design and Characterization of a Multi-Vapor Preconcentrator for a Micro-Scale Gas Chromatograph," University of Michigan, 2009.

[4] Covington, E.L. and Turner, R.W. and Kurdak, C. and Rowe, M.P. and Chao Xu and Zellers, E.T., "Electrical noise in gold nanoparticle chemiresistors," *IEEE Sensors*, pp. 102-105, Oct., 2008.

[5] C. S. Lee, F. Haghighat, W. S. Ghaly, "A study on VOC source and sink behavior in porous building materials - analytical model development and assessment," *Indoor Air*, vol. 15, no. 3, pp. 183-196, 2005.

[6] Anjali Srivastava, A. E. Joseph, S. D. Wachasunder, "Qualitative Detection of Volatile Organic Compounds in Outdoor and Indoor Air ," *Environmental Monitoring and Assessment*, vol. 96, no. 1-3, pp. 263-271, 2004.

[7] Peder Wolkoff, Thomas Schneider, Jan Kildes, Ritva Degerth, Margarethe Jaroszewski, Hannelore Schunk, "Risk in cleaning: chemical and physical exposure," *The Science of The Total Environment*, vol. 215, no. 23, pp. 135-156, 1998.

[8] Guido Fischer, Wolfgang Dott, "Relevance of airborne fungi and their secondary metabolites for environmental, occupational and indoor hygiene," *Archives of Microbiology*, vol. 179, no. 2, pp. 75-82, 2003.

[9] Jerker Fick, Calle Nilsson, Barbro Andersson, "Formation of oxidation products in a ventilation system," *Atmospheric Environment*, vol. 38, no. 35, pp. 5895-5899, 2004.

[10] L. Pommer, J. Fick, J. Sundell, C. Nilsson, M. Sjöström, B. Stenberg, B. Andersson, "Class separation of buildings with high and low prevalence of SBS by principal component analysis," *Indoor Air*, vol. 14, no. 1, pp. 16-23, 2004.

[11] Chunrong Jia, Stuart Batterman, Christopher Godwin, "VOCs in industrial, urban and suburban neighborhoods—Part 1: Indoor and outdoor concentrations, variation, and risk drivers," *Atmospheric Environment*, vol. 42, no. 9, pp. 2083-2100, 2008.

[12] A. T. Hodgson, D. Faulkner, D. P. Sullivan, D. L. DiBartolomeo, M. L. Russell and W. J. Fisk, "Effect of outside air ventilation rate on volatile organic compound concentrations in a call center," *Atmospheric Environment*, vol. 37, no. 39-40, pp. 5517-5527, 2003.

[13] http://www.cdc.gov.

[14] RA Jenkins, MR Guerin, BA Tomkins, "*The Chemistry of Environmental Tobacco Smoke: Composition and Measurement,"* New York, 2000.

[15] Sydney M Gordon, Lance A Wallace, Marielle C Brinkman, Patrick J Callahan, and Donald V Kenny, "Volatile organic compounds as breath biomarkers for active and passive smoking," *Environ Health Perspect*, vol. 110, no. 7, pp. 689-698, 2002.

[16] Roger A. Jenkins, "Performance Evaluation of Simultaneous Monitoring of Personal Exposure to Environmental Tobacco Smoke and Volatile Organic Compounds," *Indoor and Built Environment*, vol. 10, no. 3-4, pp. 200-208, 2001.

[17] Michael W. Ogden, Patricia Martin, "The use of cigarette equivalents to assess environmental tobacco smoke exposure," *Environment International*, vol. 23, no. 1, pp. 123-138, 1997.

[18] Maskarinec, M. P. Jenkins, R. A. Counts, R. W. Dindal, A. B., "Determination of exposure to environmental tobacco smoke in restaurant and tavern workers in one US city," *JOURNAL OF EXPOSURE ANALYSIS AND ENVIRONMENTAL EPIDEMIOLOGY*, vol. 10, no. 1, pp. 36-49, 2000.

[19] Wenqing Cao, Yixiang Duan, "Breath Analysis: Potential for Clinical Diagnosis and Exposure Assessment ," *Clinical Chemistry*, vol. 52, no. 5, pp. 800-811, 2006.

[20] A. McWilliams, S. Lam, "Lung cancer screening," *Current Opinion in Pulmonary Medicine*, vol. 11, no. 4, pp. 272-277, 2005.

[21] J. M. Sanchez, R. D. Sacks, "GC Analysis of Human Breath with A Series-Coupled Column Ensemble and A Multibed Sorption Trap," *Analytical Chemistry*, vol. 75, no.

10, pp. 2231-2236, 2003.

[22] Mark Libardoni, P.T. Stevens, J. Hunter Waite, Richard Sacks, "Analysis of human breath samples with a multi-bed sorption trap and comprehensive two-dimensional gas chromatography (GC × GC) ," *Journal of Chromatography B*, vol. 842, no. 1, pp. 13-21, 2006.

[23] R. F. Machado, D. Laskowski, O. Deffenderfer, T. Burch, S. Zheng, P. J. Mazzone, T. Mekhail, C. Jennings, J. K. Stoller, J. Pyle, J. Duncan, R. A. Dweik, S. C. Erzurum, "Detection of Lung Cancer by Sensor Array Analyses of Exhaled Breath ," *American Journal of Respiratory and Critical Care Medicine*, vol. 171, no. 11, pp. 1286-1291, 2005.

[24] Bureau of Alcohol Tobacco and Firearms, "Commerce in Explosives; List of Explosive Materials," *Federal Register*, vol. 67, no. 81, pp. 20864-20866, 2002.

[25] Z. Wu, C. L. Hendrickson, R. P. Rodgers, A. G. Marshall, "Composition of Explosives by Electrospray Ionization Fourier Transform Ion Cyclotron Resonance Mass Spectrometry," *Analytical Chemistry*, vol. 74, no. 8, pp. 1879-1883, 2002.

[26] D. C. Collins, M. L. Lee, "Developments in ion mobility spectrometry-mass spectrometry ," *Analytical and Bioanalytical Chemistry*, vol. 372, no. 1, pp. 66-73, 2002.

[27] X. Yang, X. Du, J. Shi, B. Swanson, "Molecular recognition and self-assembled polymer films for vapor phase detection of explosives," *Talanta*, vol. 54, no. 3, pp. 439-445, 2001.

[28] A. R. Krause, C. Van Neste, L. Senesac, T. Thundat, E. Finot, "Trace explosive detection using photothermal deflection spectroscopy," *Journal of Applied Physics*, vol. 103, no. 9, pp. 094906-094906-6, 2008.

[29] I. A. Levitsky, W. B. Euler, N. Tokranova, A. Rose, "Fluorescent polymer-porous silicon microcavity devices for explosive detection," *Applied Physics Letters*, vol. 90, no. 4, pp. 041904 - 041904-3, 2007.

[30] Deyi Kong, Tao Mei, Yongchun Tao, Lin Ni, Tao Zhang, Wei Lu, Zhengyong Zhang, Rui Wang, "A MEMS sensor array for explosive particle detection," *International Conference on Information Acquisition*, 2004.

[31] Neil S. Arnold, Jacek P. Dworzanski, Sue Anne Sheya, William H. McClennen, Henk L. C. Meuzelaar, "Design considerations in field-portable GC-based hyphenated instrumentation," *Field Analytical Chemistry & Technology*, vol. 4, no. 5, pp. 219-238, 2000.

[32] A. Keil, H. Hernandez-Soto, R. Noll, M. Fico, L. Gao, Z. Ouyan, R. G. Cooks, "Monitoring of toxic compounds in air using a handheld rectilinear ion trap mass spectrometer ," *Analytical Chemistry*, vol. 80, no. 3, pp. 734-741, 2008.

[33] A. C. Drescher, D. Y. Park, M. G. Yost, A. J. Gadgil, S. P. Levine, W. W. Nazaroff, "Stationary and time-dependent indoor tracer-gas concentration profiles measured by OP-FTIR remote sensing and SBFM-computed tomography," *Atmospheric Environment*, vol. 31, no. 5, pp. 727-740, 1997.

[34] X Liu, R Pawliszyn, L Wang, J Pawliszyn, "On-site monitoring of biogenic emissions from Eucalyptus dunnii leaves using membrane extraction with sorbent interface combined with a portable gas chromatograph system ," *The Analyst*, vol. 129, no. 1, pp. 55-62, 2004.

[35] Durana N, Navazo M, Alonso L, García JA, Ilardia JL, Gómez MC, Gangoiti G, "Online hourly determination of 62 VOCs in ambient air: system evaluation and comparison with another two analytical techniques," *Journal of the Air & Waste Management Association*, vol. 52, no. 10, pp. 1176-1185, 2002.

[36] Kevin B. Thurbide, Taylor C. Hayward, "Improved micro-flame detection method for gas chromatography ," *Analytica Chimica Acta*, vol. 519, no. 1, pp. 121-128, 2004.

[37] L. K. Whalley, A. C. Lewis, J. B. McQuaid, R. M. Purvis, J. D. Lee, K. Stemmler, C. Zellweger, P. Ridgeon, "Two high-speed, portable GC systems designed for the measurement of non-methane hydrocarbons and PAN: Results from the Jungfraujoch High Altitude Observatory ," *Journal of Environmental Monitoring*, vol. 6, no. 3, pp. 234-241, 2004.

[38] J. A. Dziuban, J. Mroz, M. Szczygielska, M. Malachowski, A. Gorecka-Drzazga, R. Walczak, W. Bula, D. Zalewski, L. Nieradko, J. Lysko, J. Koszur, P. Kowalski, "Portable gas chromatograph with integrated components," *Sensors and Actuators A: Physical*, vol. 115, no. 2,pp 318-330, 2004.

[39] P. Smith, T. Kluchinsky, P. Savage, "THEORETICAL AND EXPERIMENTAL

STUDIES-Traditional Sampling With Laboratory Analysis and Solid Phase Microextraction Sampling With Field Gas Chromatography/Mass Spectrometry by Military Industrial ," *American Industrial Hygiene Association Journal*, vol. 63, no. 3, pp. 284-292, 2002.

[40] C. Lu, Steinecker,W.H,Tian,W.C., M. Agah, J. Potkay, M. C. Oborny, J. Nichols, H. Chan, J. Driscoll, R. Sacks, S. Pang, K. Wise, E. Zellers, "First-generation hybrid MEMS gas chromatograph ," *Lab On a Chip*, vol. 5, no. 10, pp. 1123-1131, 2005.

[41] Jeongim Park, William A. Groves,Edward T. Zellers, "Vapor Recognition with Small Arrays of Polymer-Coated Microsensors. A Comprehensive Analysis," , vol. 71, no. 17, pp. 3877-3886, 1999.

[42] S. Zampolli, I. Elmi, G. Cardinali, L. Masini, A. Zani, M. Severi, P. Betti, E. Dalcanale, "A palm-sized gas-chromatographic system for sub-ppb VOC detection in air quality monitoring applications," pp. 1163 -1166, Oct 2006.

[43] C. Elosua, C. Bariain, I. Matias, F. Arregui, A. Luquin, M. Laguna, "Organic vapors detection using single mode fiber at third telecommunication window," *IEEE Sensors*, pp. 154 -157, Oct 2009.

[44] J. W. Grate, "Acoustic Wave Microsensor Arrays for Vapor Sensing," *Chemical Reviews*, vol. 100, no. 7, pp. 2627-2648, 2000.

[45] Helen C. Shields, Daniel M. Fleischer, Charles J. Weschler, "Comparisons among VOCs Measured in Three Types of U.S. Commercial Buildings with Different Occupant Densities," vol. 6, no. 1, pp. 2-17, 1996.

[46] J. Janata, "Electrochemical microsensors," *Proceedings of the IEEE*, vol. 91, no. 6, pp. 864 - 869, 2003.

[47] E. J. Severin, N. S. Lewis, "Relationships among Resonant Frequency Changes on a Coated Quartz Crystal Microbalance, Thickness Changes, and Resistance Responses of Polymer Carbon Black Composite Chemiresistors," *Analytical Chemistry*, vol. 72, no. 9, pp. 2008-2015, 2000.

[48] H. Wohltjen, A. W. Snow, "Colloidal Metalâˆ’Insulatorâˆ’Metal Ensemble Chemiresistor Sensor," *Analytical Chemistry*, vol. 70, no. 14, pp. 2856-2859, 1998.

[49] H. Chang, S. Kim, T. Sukaew, F. Bohrer, W. Zellers, "Microfabricated gas chromatograph for Sub-ppb determinations of TCE in vapor intrusion investigations," *Procedia Engineering*, vol. 5, pp. 973-976, 2010.

[50] W. H. Steinecker, M. P. Rowe, E. T. Zellers, "Model of Vapor-Induced Resistivity Changes in Goldâˆ’Thiolate Monolayer-Protected Nanoparticle Sensor Films," *Analytical Chemistry*, vol. 79, no. 13, pp. 4977-4986, 2007.

[51] A. Flammini, D. Marioli, A. Taroni, "A low-cost interface to high-value resistive sensors varying over a wide range," *IEEE Transactions on Instrumentation and Measurement*, vol. 53, no. 4, pp. 1052 - 1056, 2004.

[52] http://www.analog.com/en/analog-to-digital-converters/ad-converters/products/index.html#All_ADCs.

[53] M. Grassi, P. Malcovati, A. Baschirotto, "A 141-dB Dynamic Range CMOS Gas-Sensor Interface Circuit Without Calibration With 16-Bit Digital Output Word," *IEEE Journal of Solid-State Circuits*, vol. 42, no. 7, pp. 1543 -1554, 2007.

[54] Haiqi Liu, Tee Hui Teo, Yue Ping Zhang, "A low-power wide-range interface circuit for nanowire sensor array based on resistance-to-frequency conversion technique," pp. 13-16, Dec 2009.

[55] M. Malfatti, M. Perenzoni, N. Viarani, A. Simoni, L. Lorenzelli, A. Baschirotto, "A complete front-end system read-out and temperature control for resistive gas sensor array," *Proceedings of European Conference on Circuit Theory and Design*, 2005.

[56] S. Bagga, N. Bhat, S. Mohan, "LPG Gas-Sensing System With SnO2 Thin-Film Transducer and 0.7um CMOS Signal Conditioning ASIC," *Instrumentation and Measurement, IEEE Transactions on*, vol. 58, no. 10, pp. 3653 -3658, 2009.

[57] N. Bhat, B. Jayaraman, R. Pratap, S. Bagga, S. Mohan. Integrated CMOS gas sensors. In *Electron devices and semiconductor technology, 2009. iedst '09. 2nd international workshop on*. 2009.

[58] D. Barrettino, M. Graf, S. Taschini, S. Hafizovic, C. Hagleitner, A. Hierlemann, "CMOS Monolithic Metal Oxide Gas Sensor Microsystems," *Sensors Journal, IEEE*, vol. 6, no. 2, pp. 276 - 286, 2006.

[59] M. Grassi, P. Malcovati, A. Baschirotto, "A 160 dB Equivalent Dynamic Range Auto-Scaling Interface for Resistive Gas Sensors Arrays," *Solid-State Circuits, IEEE Journal of*, vol. 42, no. 3, pp. 518 -528, 2007.

[60] Thomas Jacob Koickal, Alister Hamilton, Su Lim Tan, James A. Covington, Julian W. Gardner, Tim C. Pearce, "Analog VLSI Circuit Implementation of an Adaptive Neuromorphic Olfaction Chip," *Circuits and Systems I: Regular Papers, IEEE Transactions on*, vol. 54, no. 1, pp. 60-73, 2007.

[61] C. Leung, D. Wilson, "Integrated interface circuits for chemiresistor arrays," *IEEE Circuits and Systems International Symposium on*. 2005.

[62] D. Rairigh, G. Warnell, Chao Xu, E. Zellers, A. Mason, "CMOS Baseline Tracking and Cancellation Instrumentation for Nanoparticle-Coated Chemiresistors," *Biomedical Circuits and Systems, IEEE Transactions on*, vol. 3, no. 5, pp. 267 -276, 2009.

[63] Kuo-Jung Wang, Fan-Chung Tseng, Wei-Lin Chen, Guang-Ren Shen, Wang, W.W., Lee, K., "Analysis of Radiation Damage on a Monolithic CMOS-MEMS Printhead," *EDSSC*, pp. 293-295, , 2007.

[64] Campabadal F., Ghatnekar-Nilsson S., Rius G., Figueras E., Esteve J., "Nanocantilevers with integrated CMOS Effects of EBL on NMOS transistors," *Spanish Conference on Electron Devices*, pp. 213-216, 2005.

[65] Daniel J. Rairigh, "IMPEDANCE SPECTROSCOPY WITH BASELINE CANCELLATION FOR BIOCHEMICAL SENSOR ARRAYS," 2011 (To be expected).

[66] C. C. Enz and G. C. Temes, "Circuit techniques for reducing the effects of op-amp imperfections: autozeroing, correlated double sampling, and chopper stabilization," *Proc. IEEE*, vol. 84, pp. 1584-1614, 1996.

[67] Chao Yang, Sachin R. Jadhav, R. Mark Worden, and Andrew J. Mason, "Compact low-power impdeance-to-digital converter for sensor array microsystems," *IEEE Journals of Solid-State Circuits*, vol. 44, pp. 2844-2855, 2009.